On the relationship between solid particle attractors and thermal inhomogeneities in vibrationally driven fluid-particle systems (EP)

View Online   Export Citation   CrossMark

Balagopal Manayil **Santhosh** (बालगोपाल संतोष), (iD) and Marcello Lappa[a] (iD)

AFFILIATIONS

Department of Mechanical and Aerospace Engineering, University of Strathclyde, James Weir Building, 75 Montrose Street, Glasgow
G1 1XJ, United Kingdom

[a]Author to whom correspondence should be addressed: marcello.lappa@strath.ac.uk

ABSTRACT

The present analysis extends earlier authors' work [Crewdson et al., "Two-dimensional vibrationally-driven solid particle structures in non-uniformly heated fluid containers," Chaos **32**, 103119 (2022); M. Lappa, "Characterization of two-way coupled thermovibrationally driven particle attractee," Phys. Fluids **34**(5), 053109 (2022); M. Lappa and T. Burel, "Symmetry breaking phenomena in thermovibrationally driven particle accumulation structures," ibid. **32**(5), 053314 (2020); and M. Lappa, "The patterning behavior and accumulation of spherical particles in a vibrated non-isothermal liquid," ibid. **26**(9), 093301 (2014)] on the existence of solid particle attractee in thermovibrational flow in order to identify new physical principles and enable increased control over the ability of particles to target desired locations into the host fluid. The causality between the thermal boundary conditions and the multiplicity and morphology of emerging particle structures is discussed, and new fundamental topological concepts are harnessed through the combination of two-dimensional and three-dimensional simulations. It is shown that the threefold relationship among the inclination of vibrations, the multi-directional nature of the imposed temperature gradient, and the dimensionality of the system itself can open up new pathways for additional classes of attractors. These can manifest themselves as compact particle structures or completely disjoint sets, apparently behaving as they were driven by different clustering mechanisms (coexisting in the physical space, but differing in terms of characteristic size, shape, and position). A variety of new solutions are presented for a geometry as simple as a cubic enclosure in the presence of localized spots of temperature on otherwise uniformly heated or cooled walls. In order to filter out possible asymmetries due to fluid-dynamic instabilities induced by the back influence of the solid mass on the fluid flow, the analysis is conducted under the constraint of one-way coupled phases.

I. INTRODUCTION

Many "fluid" materials with industrial relevance such as suspensions, emulsions, foams, wet granular (dense) media, and (dilute) dispersions of different types consist of a minority phase dispersed into a majority phase. Different levels of "interaction" among these "components" are possible according to the considered conditions; the minority elements can undergo reciprocal or mutual interference and/or exchange mass, momentum, and energy with the surrounding phase via various mechanisms.

Multiphase systems of such a kind can be found in several areas, e.g., materials,[1] nuclear,[2,3] chemical,[4] pharmaceutical,[5] and food engineering,[6] just to cite a few. Superimposed on their variety (depending on the specific nature of the considered minority and majority phases

and the degree of dilution of the former), an additional factor contributing to make this field vast is the wide range of scales that these processes can cover (going from few micrometers to several meters and even larger lengths if certain phenomena occurring in nature are also included in the discussion[7,8]).

Remarkably, the industrial relevance of these facts, in conjunction with the appeal that the related spatiotemporal behaviors exert on scholars at a more fundamental level, has stimulated the development of dedicated experimental and theoretical lines of inquiry, and resulted in a sound understanding of the underlying cause-and-effect relationships.[7,9–14]

Owing to space limitations, we do not strive to review all the aspects of the existing research on these subjects. Rather, we

concentrate on a relatively recent avenue where new principles to design novel particle management technologies in fluid flow have been sought by leveraging the spontaneous ability of solid particles to undergo separation, sorting, and accumulation due to their *inertial properties* (finite size and mass). While many features of dense particle-fluid systems heavily driven by particle–particle interactions are still mysterious and require models that have not been elaborated yet,[15] the mechanism by which inertial particles hosted in a liquid can evolve from an initial uniform or random dispersion to non-trivial states (characterized by a certain degree of self-organization) is reasonably well understood and uncontroversial.

Most importantly, these processes are also enabled in dilute systems and, as such, are much more general and universally applicable. The simplest way to introduce them, perhaps, is to consider that, because of their physical nature (non-zero mass and non-negligible size), solid particles are not forced to follow passively the fluid streamlines. The drag that the fluid exerts on the dispersed solid matter and its different density with respect to the fluid itself can cause dynamic "disturbances" by which the particles are allowed to develop an "independent" velocity field; as an example, their velocity can violate the constraint of incompressibility, which instead applies to the carrier fluid flow. Owing to this effect, the paths of the solid particles become intertwined and the spacing among them can change; thereby, particles are allowed to demix from the fluid and concentrate in specific subregions of the considered spatial domain. Existing analyses have shown that, however, the topology of the carrier flow still plays a role in such dynamics as the existence of closed paths or repetitive behaviors can serve as "sinks," i.e., give rise to attracting loci where particles tend to concentrate as the aforementioned compressibility effects or disturbances accumulate in time.[7,16,17]

The temporal nature of the fluid flow itself does also matter. As an example, while, due to the small-scale nature of the temporal fluctuations occurring in turbulent flows, particles simply form small aggregates with relatively irregular shapes,[18,19] much more ordered and (spatially) extended formations can be obtained in the situations where the flow is time-periodic. This is the case for instance of the tracer particles dispersed in liquid bridges when the surface-tension-driven (Marangoni) flow becomes oscillatory due to the excitation of hydrothermal waves (first Hopf bifurcation[20–26]).

This is also the case, when a time-periodic mode of convection is obtained by imposing a suitable external "forcing," and a relevant example is represented by the situation where vibrations are applied to a non-isothermal incompressible fluid in microgravity conditions. Obviously, in this specific case (the main subject of analysis here), particle attractors still obey the general "compressibility principles" elucidated above; i.e., the density of particles and of the fluid must be different.

Nevertheless, a hallmark inherent to this specific class of particle structures is their *extreme regularity* and the ability to take different three-dimensional (3D) shapes depending on the inclination of vibrations with respect to the direction of the imposed temperature gradient (as opposed to the essentially one-dimensional nature of the particle circuits formed in the aforementioned Marangoni flow case). Most surprisingly, these shapes have been found to mimic closely the family of "quadric" surfaces of projective geometry.[27–30]

The related properties have already been extensively described in earlier studies and have been the main subject of an experiment conducted in space.[31] For the convenience of the reader, here we limit ourselves to recalling that, from a purely mathematical point of view, such geometrical surfaces can be defined as loci of points in a three-dimensional space implicitly described by a polynomial equation of degree 2. Put simply, they may be regarded as generalizations of two-dimensional conic sections (ellipses, parabolas, and hyperbolas) in 3D. In particular, Lappa and co-workers could effectively find accumulation structures of such a kind (i.e., ellipsoids, paraboloids, hyperboloids, and cylindrical and conical surfaces) in the framework of numerical studies based on the so-called one-way coupled Eulerian–Lagrangian approach.[27–30]

We wish also to highlight that these findings have been obtained for simplified (easy to handle) fluid-dynamic configurations, namely, geometries as simple as a cubic cavity with relatively simple thermal boundary conditions, intentionally adopted to reveal the behavior of these systems in response to changes of some parameters (the magnitude, frequency and direction of vibrations, and the inertial properties of the dispersed phase). In other words, research up until this point has not yet branched out to irregularly heated configurations. The only exception is represented by the earlier investigation by Crewdson *et al.*,[32] where a temperature varying along different directions was considered in place of a unidirectional temperature gradient; in particular, it was illustrated that the multiplicity of the attracting loci in a square cavity can be increased proportionally to the number of inversions in the direction of the imposed temperature gradient.

Although interesting in its findings and in terms of the promising direction indicated about possible ways to expand the current knowledge on these phenomena, this reference, however, was limited to the two-dimensional physical space. For this reason, the present investigation proceeds one step further and addresses the fully three-dimensional case under the effect of a multi-directional temperature gradient. The study is carried out with the specific intent to collect new observational information, which will play a key role in supporting current efforts to develop a new generation of Artificial Intelligence (AI) algorithms to allow for additional impact of this line of research. More precisely, the long-term objective is the implementation of reversed input–output cause-and-effect relationship by which (after proper "training") an AI algorithm will be in a condition to return the set of thermal boundary conditions required to obtain particle accumulations with desired (fixed "a priori") multiplicity, morphology, and size. This will open vast perspectives for the production of new materials in space with properties that cannot be obtained in normal gravity conditions, relevant examples being metal or plastic alloys where the position of the minority phase can be controlled precisely and even forced to form well-defined internal structures or "frameworks." Possible applications (just to cite a few) could be special metal alloys[33,34] characterized by an internal skeleton or backbone able to address stresses or forces acting in specific directions or nonmetallic materials able to conduct electricity (e.g., a framework of metal particles in a non-conducting materials such as plastic or glass). Other relevant applications can also be envisaged in the pharmaceutical field, where protein crystals are typically obtained as seeds in an external liquid solution[35,36] and the position and aggregation of such seeds is of crucial importance with regard to the quality of the final crystals that can be produced with these techniques.

II. MATHEMATICAL MODEL

A. Considered geometry and related thermal boundary conditions

As the present article builds on and, at the same time, it seeks to extend the earlier knowledge accumulated over recent years on these topics, we consider once again the classical cubic cavity in weightless conditions with side having length L examined by Lappa,[27–29] Lappa and Burel,[30] and Crewdson and Lappa[37] (no gravity being present, which would otherwise dominate the considered dynamics). As the main motivation for reexamining this kind of problems is the recent discovery of new morphologies in terms of particle structures and related changes in the multiplicity of the attracting loci,[32] a rational generalization of those findings is sought. While the above-mentioned previous 3D studies were limited to configurations with a hot face and an opposite cold face, here the situation is examined where the temperature on such walls is not uniform. More specifically, following Crewdson et al.,[32] we focus on the circumstances where each of the two opposing thermally controlled walls displays a central patch with a different temperature as indicated in Fig. 1.

The distinguishing mark with respect to the earlier study by Crewdson et al.[32] is obviously represented by the finite extension of these patches in the spanwise direction (each patch may be regarded as a square thermal spot centrally placed into a larger hosting wall with different temperatures). All the other boundaries are thermally insulated.

B. Driving force and governing equations for the fluid phase

As an extended derivation or description of the governing equations for the fluid phase has been repeatedly reported in

FIG. 1. Sketch of the considered thermal boundary conditions: two thermally controlled opposing walls are set at a temperature T_{cold} and T_{hot}, respectively; each wall, however, is featured by a centrally located square spot having the same temperature of the opposing wall.

Refs. 27–30, 32, and 37, it is not duplicated here. In this section, we limit ourselves to recalling that vibrations can be mathematically modeled as a sinusoidal displacement varying with time, defined by an amplitude b (m) and an angular frequency ω (rad/s), where $\omega = 2\pi f$ and f is the frequency in hertz. Such a sinusoidal displacement dynamically enforces an acceleration $g(t)$ varying with the same sinusoidal law in time and an amplitude given by the product of b and the square of the angular frequency, i.e., $b\omega^2$.[14,38] This dynamical effect can be directly incorporated into the momentum balance equation through the standard Boussinesq approximation valid for liquids. The flow driving force, therefore, reduces to a source term $\rho g(t)$ at the right-hand side of this equation where the fluid density ρ is replaced by a simplified expression by which it is assumed to scale linearly with the temperature.

In this framework, the governing mass, momentum, and energy equations for the fluid phase can therefore be cast in compact non-dimensional form, respectively, as

$$\nabla \cdot \underline{V} = 0, \tag{1}$$

$$\frac{\partial \underline{V}}{\partial t} = -\nabla p - \nabla \cdot [\underline{V}\,\underline{V}] + \mathrm{Pr}\nabla^2 \underline{V} - \mathrm{Pr}Ra_\omega T \sin(\Omega t)\hat{\underline{n}}, \tag{2}$$

$$\frac{\partial T}{\partial t} + \nabla \cdot [\underline{V}T] = \nabla^2 T, \tag{3}$$

where $\underline{V}$, p, and T are the non-dimensional velocity (with components u, v, and w along x, y, and z, respectively), pressure, and temperature. In doing so, we have implicitly assumed that the reference quantities for all lengths, the velocity, the time, the pressure, and the temperature are the size of the cavity (L), (α/L), (L^2/α), ($\rho\alpha^2/L^2$), and $\Delta T = T_{hot} - T_{cold}$ respectively. The characteristic numbers appearing in these equations represent effective degrees of freedom of the considered system in terms of possible fluid-dynamic behaviors. These are

$$\mathrm{Pr} = \frac{\nu}{\alpha}, \tag{4}$$

i.e., the well-known Prandtl number (where ν is the fluid kinematic viscosity given by the ratio of dynamic viscosity and fluid density, i.e., $\nu = \mu/\rho$ and α is the fluid thermal diffusivity). Moreover, Ra_ω appearing in the buoyancy term is the vibrational Rayleigh number, analogue to the classical Rayleigh number used in standard gravitational convection problems (Ra), namely,

$$Ra_\omega = \frac{(b\omega^2 \beta_T \Delta T L^3)}{\nu\alpha}, \tag{5}$$

where β_T is the fluid thermal expansion coefficient. Finally, Ω is the non-dimensional angular frequency of the vibrations defined as

$$\Omega = \frac{\omega L^2}{\alpha} = \frac{2\pi}{P}, \tag{6}$$

where P is the non-dimensional period of vibrations.

C. The minority phase

In line with the majority of research on this specific subject, which has been based on a model that describes the fluid behavior using classical fluid mechanics, i.e., the aforementioned Navier–Stokes equations (1)–(3) and the particle dynamics in the
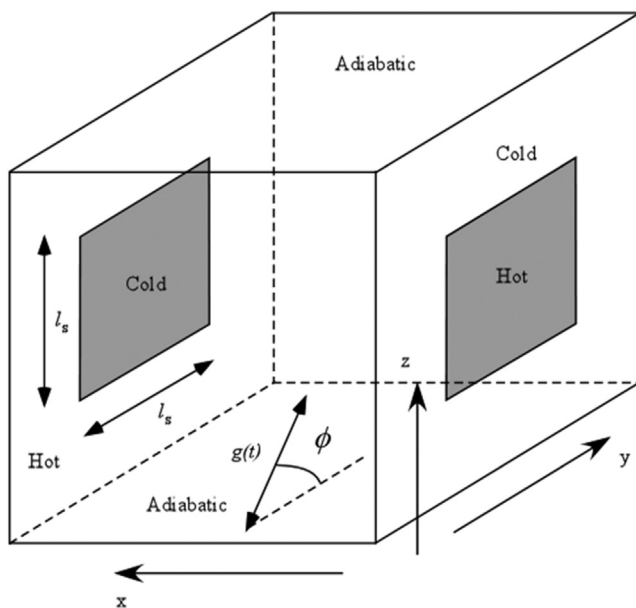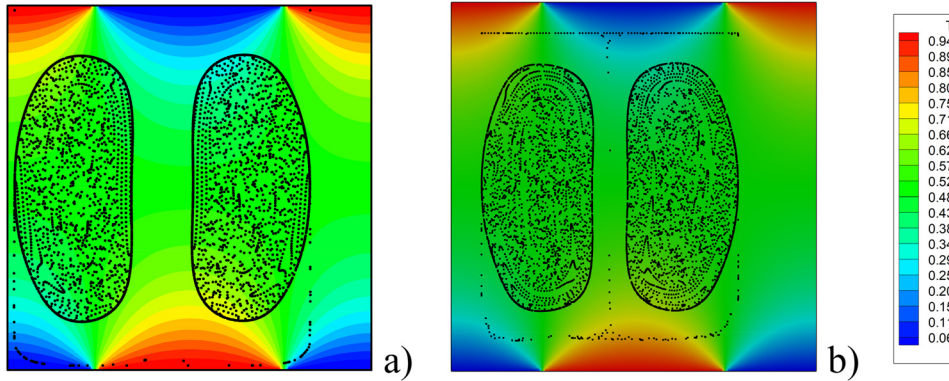
FIG. 2. Comparison of numerical results (one-way coupling) obtained with the present computational platform and OpenFOAM for $l_s = 0.5$, Pr $= 6.1$, $\gamma = 10^8$, $Ra_\omega = 10^4$, $\Omega = 10^3$, $St = 5 \times 10^{-6}$, and $\xi = 2$ at $t \cong 6.55$ (the slightly different colors are due to the different post-processing software used to visualize the results yielded by the two considered computational platforms).

framework of a segregated (but properly coupled) Lagrangian approach, here we resort to a one-way coupled strategy.[27–30] This means that solid particles do not influence the carrier flow and are used solely to reveal the properties of the underlying attractee, which in this case behave as undisturbed templates for the accumulation of particles (the ability of the dispersed mass to induce asymmetries and other effects in the otherwise undisturbed flow has already been explored in an earlier work,[39] to which the interested reader is referred).

The transport equation for the solid particles accordingly reads

$$\frac{d\underline{V}p}{dt} = \frac{1}{\xi + 1/2}\left[-\frac{\mathrm{Pr}}{St}f(\mathrm{Re}_p)\left(\underline{V}_p - \underline{V}\right) + \frac{3}{2}\frac{d\underline{V}}{dt} \right.$$
$$\left. + \frac{3}{2}\left(\underline{V} \cdot \underline{\nabla}\,\underline{V}\right)\right] + \frac{\xi-1}{\xi + 1/2}\gamma \sin\left(\Omega t\right)\hat{\underline{n}}, \qquad (7)$$

where the additional non-dimensional parameter γ reads

$$\gamma = \frac{b\omega^2 L^3}{\alpha^2}, \qquad (8)$$
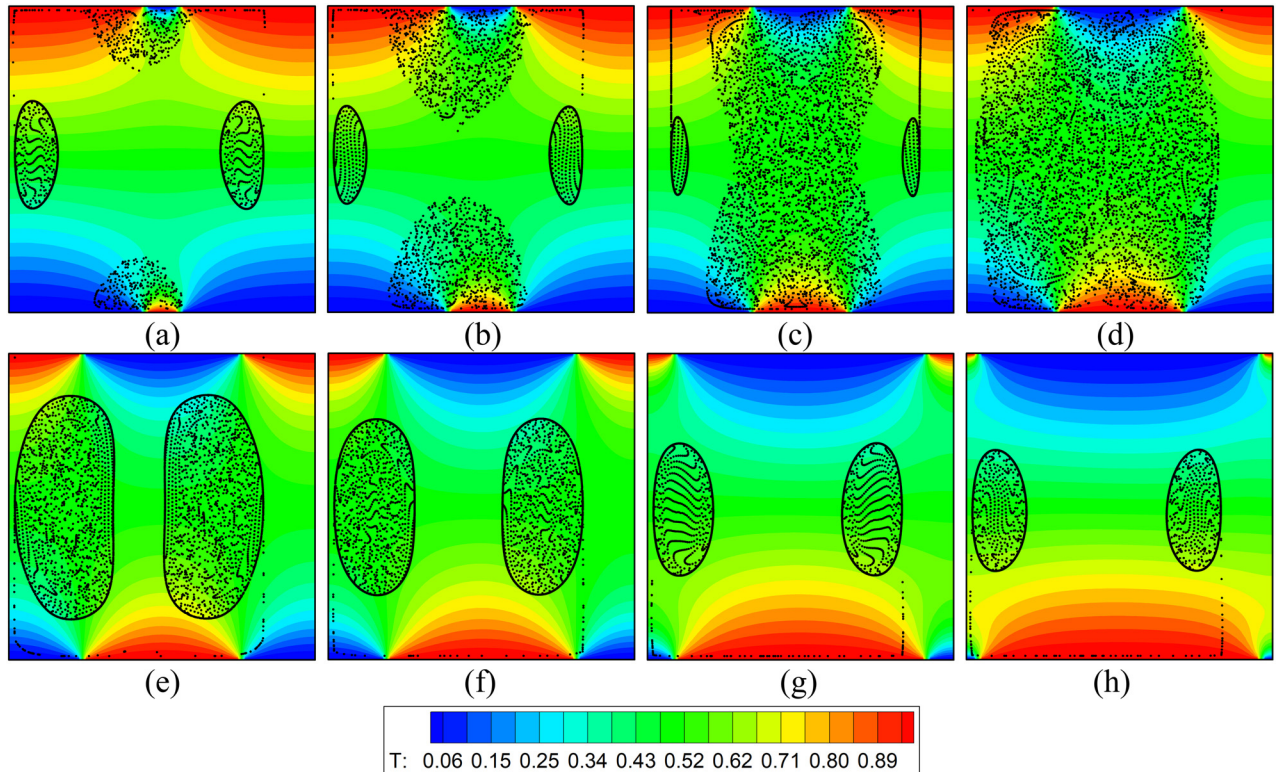

FIG. 3. Snapshots of temperature field and particle distribution (2D computations) for $\gamma = 10^8$, $Ra_\omega = 10^4$, $\Omega = 10^3$, $St = 5 \times 10^{-6}$ and $\xi = 2$ at $t \cong 6.55$: (a) $l_s = 0.1$, (b) $l_s = 0.2$, (c) $l_s = 0.3$, (d) $l_s = 0.4$, (e) $l_s = 0.5$, (f) $l_s = 0.6$, (g) $l_s = 0.8$, (h) $l_s = 0.9$.
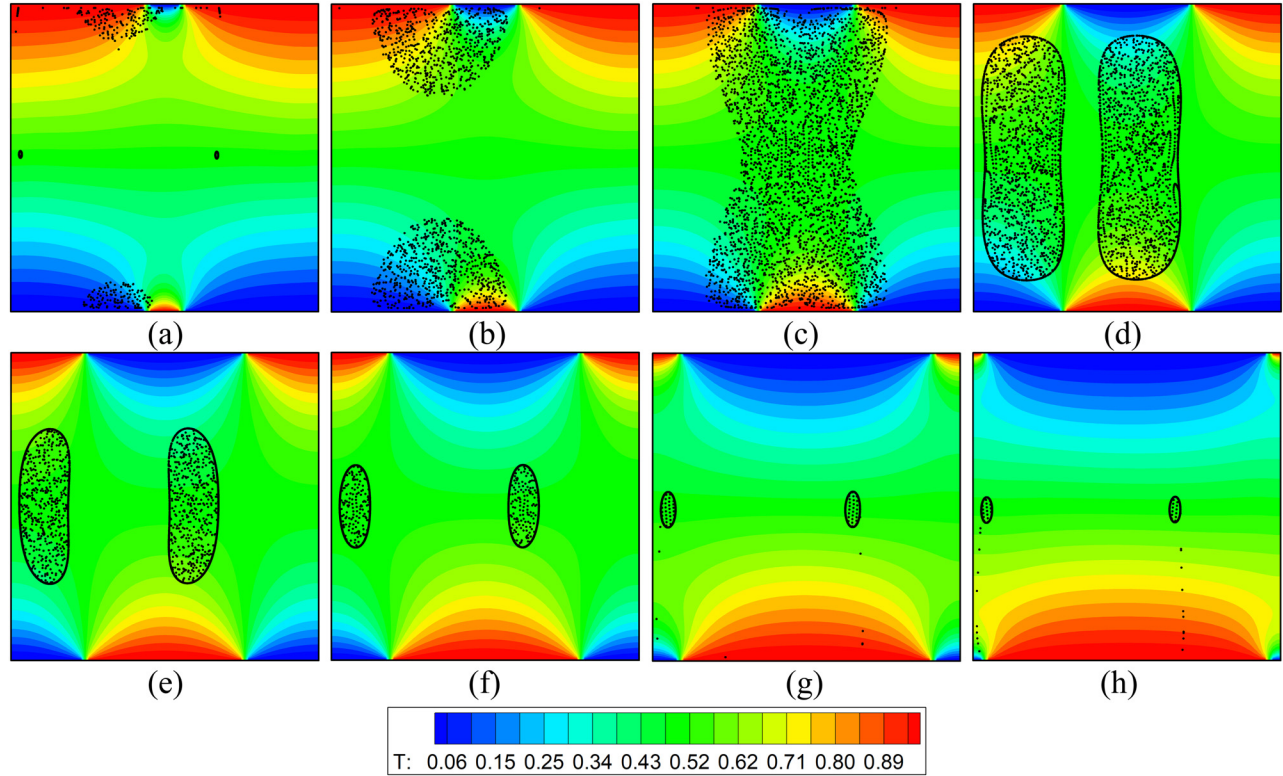
FIG. 4. Snapshots of temperature field and particle distribution (2D computations) for $\gamma = 2 \times 10^8$, $Ra_\omega = 10^4$, $\Omega = 10^3$, $St = 5 \times 10^{-6}$, and $\xi = 2$ at $t \cong 6.55$: (a) $l_s = 0.1$, (b) $l_s = 0.2$, (c) $l_s = 0.3$, (d) $l_s = 0.4$, (e) $l_s = 0.5$, (f) $l_s = 0.6$, (g) $l_s = 0.8$, (h) $l_s = 0.9$.

and it accounts for the non-dimensional amplitude of the acceleration induced by vibrations. Moreover, $\underline{V}_p = [u_p, v_p, w_p]$ is the particle velocity and $f(\mathrm{Re}_p)$ is a corrective factor required to account for the departure of the drag from the classical Stokes law,[40]

$$f(\mathrm{Re}_p) = 1 + 0.15\mathrm{Re}_p^{0.687}, \tag{9}$$

where Re_p is the particle instantaneous Reynolds number, defined as

$$\mathrm{Re}_p = \frac{2R_p\rho|\underline{V} - \underline{V}p|}{\mu}. \tag{10}$$

Moreover, the particle to fluid density ratio ξ and the Stokes number St appearing in Eq. (7) read
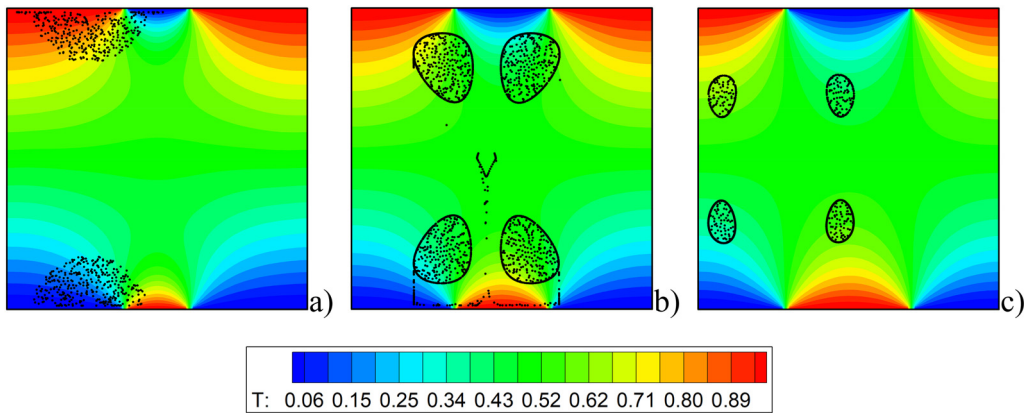

FIG. 5. Snapshots of temperature field and particle distribution (2D computations) for $\gamma = 3 \times 10^8$, $Ra_\omega = 10^4$, $\Omega = 10^3$, $St = 5 \times 10^{-6}$ and $\xi = 2$ at $t \cong 6.55$: (a) $l_s = 0.2$, (b) $l_s = 0.3$, (c) $l_s = 0.4$.
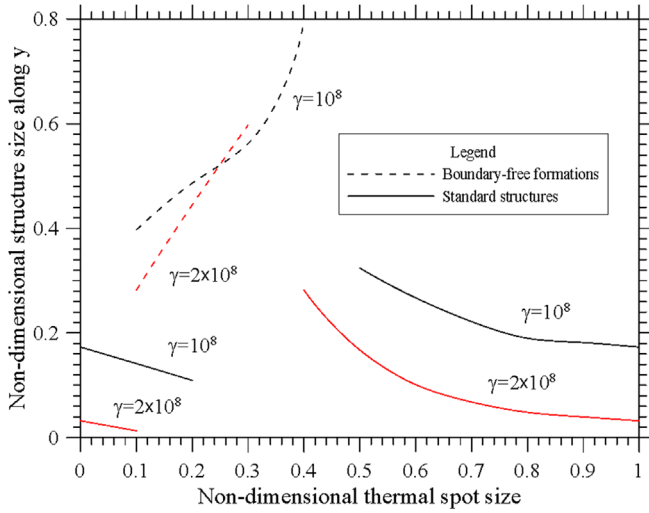
FIG. 6. Characteristic size along y (direction of imposed vibrations) of the emerging structures for different values of the spot size l_s (2D computations for $Ra_\omega = 10^4$, $\Omega = 10^3$, $St = 5 \times 10^{-6}$, and $\xi = 2$; the splines are used to guide the eye; the solid and dashed lines refer to the standard and boundary-free formations, respectively; black color—$\gamma = 10^8$; red color—$\gamma = 2 \times 10^8$).

FIG. 7. Characteristic size along x of the emerging structures for different values of the spot size l_s (2D computations for $Ra_\omega = 10^4$, $\Omega = 10^3$, $St = 5 \times 10^{-6}$ and $\xi = 2$; the splines are used to guide the eye; the solid and dashed lines refer to the standard and boundary-free formations, respectively; black color—$\gamma = 10^8$; red color—$\gamma = 2 \times 10^8$).
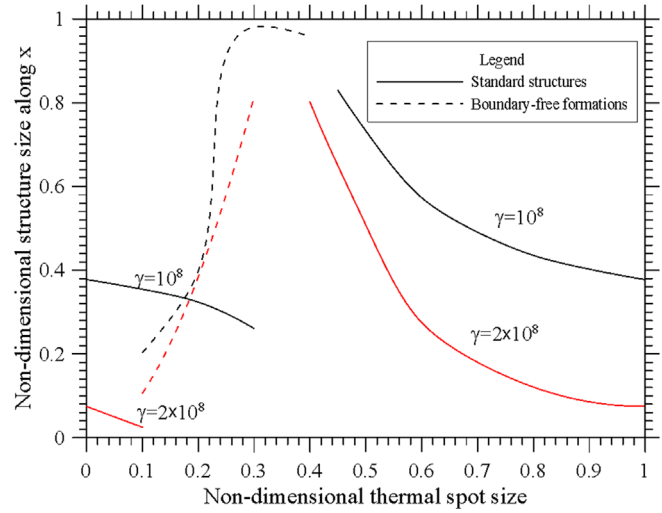
$$\xi = \rho_P / \rho, \tag{11}$$

$$St = \frac{2}{9} \frac{R_P^2}{L^2}, \tag{12}$$

where R_p is the particle radius.

A transport equation for the particle internal energy is not considered in the present work as the heat exchange between the two involved solid and liquid phases is neglected (solid phase is considered in thermal equilibrium with the liquid), the interested reader being referred to Lappa[39] for a critical discussion and quantitative assessment of the implications and reliability of this assumption.

D. Boundary conditions

The boundary conditions for the solid walls read

$$\partial T / \partial y = 0 \quad \text{and} \quad \underline{V} = 0 \text{ for } y = 0,$$
$$y = 1, 0 \leq x \leq 1, 0 \leq z \leq 1, \quad \text{and} \quad t \geq 0, \tag{13}$$

$$\partial T / \partial z = 0 \quad \text{and} \quad \underline{V} = 0 \text{ for } z = 0,$$
$$z = 1, 0 \leq x \leq 1, 0 \leq y \leq 1, \quad \text{and} \quad t \geq 0, \tag{14}$$

$$T = 0 \quad \text{and} \quad \underline{V} = 0 \text{ for } x = 0, 0 \leq y \leq 1,$$
$$0 \leq z \leq \tfrac{1}{2}(1 - l_s), \quad \text{and} \quad t \geq 0, \tag{15a}$$

$$T = 0 \quad \text{and} \quad \underline{V} = 0 \text{ for } x = 0, 0 \leq y \leq \tfrac{1}{2}(1 - l_s),$$
$$\tfrac{1}{2}(1 - l_s) \leq z \leq \tfrac{1}{2}(1 + l_s), \quad \text{and} \quad t \geq 0, \tag{15b}$$

$$T = 0 \quad \text{and} \quad \underline{V} = 0 \text{ for } x = 0, \tfrac{1}{2}(1 + l_s) \leq y \leq 1,$$
$$\tfrac{1}{2}(1 - l_s) \leq z \leq \tfrac{1}{2}(1 + l_s) \quad \text{and} \quad t \geq 0, \tag{15c}$$

$$T = 0 \quad \text{and} \quad \underline{V} = 0 \text{ for } x = 0, 0 \leq y \leq 1,$$
$$\tfrac{1}{2}(1 + l_s) \leq z \leq 1 \quad \text{and} \quad t \geq 0, \tag{15d}$$

$$T = 1 \quad \text{and} \quad \underline{V} = 0 \text{ for } x = 0,$$
$$\tfrac{1}{2}(1 - l_s) \leq y \leq \tfrac{1}{2}(1 + l_s),$$
$$\tfrac{1}{2}(1 - l_s) \leq z \leq \tfrac{1}{2}(1 + l_s), \quad \text{and} \quad t \geq 0, \tag{15e}$$

$$T = 1 \quad \text{and} \quad \underline{V} = 0 \text{ for } x = 1, 0 \leq y \leq 1,$$
$$0 \leq z \leq \tfrac{1}{2}(1 - l_s), \quad \text{and} \quad t \geq 0, \tag{16a}$$

$$T = 1 \quad \text{and} \quad \underline{V} = 0 \text{ for } x = 1, 0 \leq y \leq \tfrac{1}{2}(1 - l_s),$$
$$\tfrac{1}{2}(1 - l_s) \leq z \leq \tfrac{1}{2}(1 + l_s), \quad \text{and} \quad t \geq 0, \tag{16b}$$

$$T = 1 \quad \text{and} \quad \underline{V} = 0 \text{ for } x = 1, \tfrac{1}{2}(1 + l_s) \leq y \leq 1,$$
$$\tfrac{1}{2}(1 - l_s) \leq z \leq \tfrac{1}{2}(1 + l_s), \quad \text{and} \quad t \geq 0, \tag{16c}$$

$$T = 1 \quad \text{and} \quad \underline{V} = 0 \text{ for } x = 1, 0 \leq y \leq 1,$$
$$\tfrac{1}{2}(1 + l_s) \leq z \leq 1, \quad \text{and} \quad t \geq 0, \tag{16d}$$

$$T = 0 \quad \text{and} \quad \underline{V} = 0 \text{ for } x = 1, \tfrac{1}{2}(1 - l_s) \leq y \leq \tfrac{1}{2}(1 + l_s),$$
$$\tfrac{1}{2}(1 - l_s) \leq z \leq \tfrac{1}{2}(1 + l_s), \quad \text{and} \quad t \geq 0. \tag{16e}$$

III. THE NUMERICAL METHOD

A. The standard projection technique for fluid flow

This class of numerical techniques is heavily reliant on the coupling between pressure and velocity (which explains why methods of such a kind are generally indicated as pressure solvers in most of existing commercial CFD packages).

The numerical problem is formulated and solved in a multistage form. More precisely, the associated time-marching algorithm is structured around the main objective of systematically integrating an alternate set of equations (equivalent to the original set of mass and momentum balance equations from a mathematical point of view, but not from a numerical standpoint[41]) in order

to obtain a velocity field that satisfies at the same time the incompressibility constraint and the momentum equation.

This approach relies on physical and mathematical principles involving well-posedness theory, which are keys to the physically consistent and computationally reliable method derivation.[42] From a purely practical standpoint, they are reverberated into a procedure articulated into three fundamental steps or stages of calculation.

In step 1, the momentum is initially integrated in a simplified (unphysical) form where the pressure (gradient) term is not included in order to allow a straightforward derivation of a new velocity field as a function of the related value known at a given time instant. This is achieved considering the following equation:

$$\frac{\partial \underline{V}^*}{\partial t} = \left[-\underline{\nabla} \cdot [\underline{V}\,\underline{V}] + \mathrm{Pr}\nabla^2 \underline{V} - \mathrm{Pr}Ra_\omega T \sin(\Omega t)\hat{\underline{n}} \right], \quad (17)$$

where the first, the second, and third terms on the left-hand side represent the convective transport, diffusive transport, and production of momentum, respectively (but the pressure term is not present, as explained before).

The physical significance of the velocity is then recovered by reintroducing the previously disregarded pressure term, which leads to a correction equation, formally expressed as

$$\underline{V} = \underline{V}^* - \Delta t\,\underline{\nabla}\,p. \quad (18)$$

Substitution of this corrected formula into the mass balance equation, i.e., Eq. (1), leads to another equation required for the execution of the second stage of calculation, namely, the so-called pressure equation, which, with simple mathematical manipulations, can be cast in compact form as
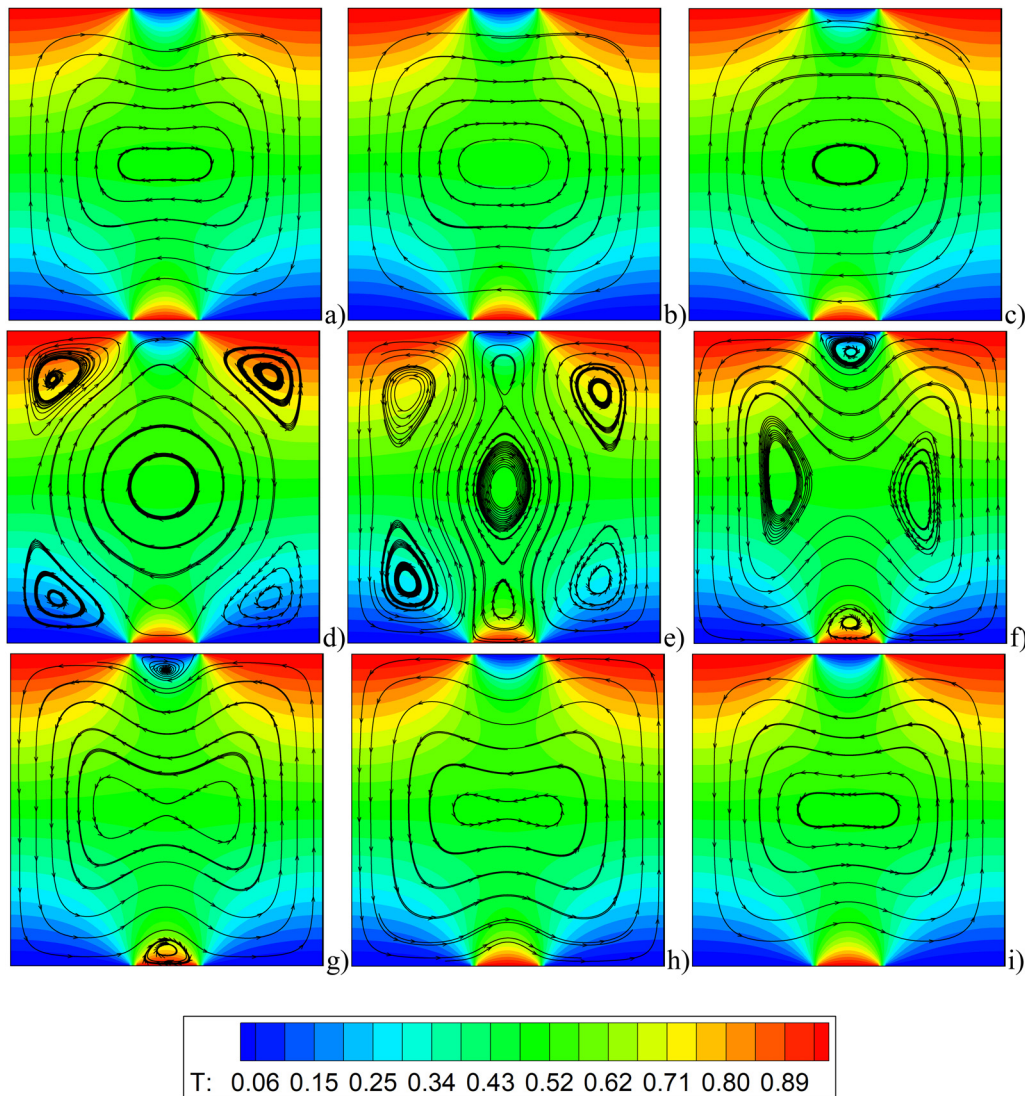

FIG. 8. Nine snapshots of temperature and streamlines evenly spaced within half of the forcing period $P = 2\pi/\Omega$ for $Ra_\omega = 10^4$, $\Omega = 10^3$, and $l_s = 0.2$ (2D computations).

$$\nabla^2 p = \frac{1}{\Delta t} \underline{\nabla} \cdot \underline{V}^*. \tag{19}$$

As the reader will realize by examining the mathematical shape of the related terms, Eqs. (17) and (19) are parabolic and elliptic in nature, respectively. These two equations are typically solved using the effective fluid velocity on the boundary for Eq. (17) (i.e., Dirichlet condition corresponding to no-slip walls in the present case) and homogeneous Neumann boundary conditions ($\partial p/\partial n = 0$, where n indicates the direction perpendicular to the solid wall) for Eq. (19), respectively. Equation (18) formally closes the loop by providing an expression for the calculation of the final (physically consistent) velocity after the intermediate velocity $\underline{V}^*$ and p have been determined. Given the weak magnitude of the fluid flow involved in the present problem,[39] standard central differences have been used to discretize both convective and diffusive terms appearing in Eq. (17). The required grids have been selected on the basis of the criteria illustrated by Lappa[43] (80 computational nodes evenly spaced along each spatial direction, reflecting the well-known and fortunate absence of boundary layers in thermovibrational flow for the conditions considered in the present work).

The velocity obtained in such a way is used to determine the contribution appearing at the right-hand side of Eq. (7). As these need to be evaluated at the instantaneous particle position, in turn, this leads to the need for relevant interpolation schemes to reconstruct the value of the velocity and its derivatives at this location starting from the known nodal values in grid points located in a given neighborhood of the particle. In the present case, simple linear interpolations have been employed. The particle-tracking Lagrangian equation has been integrated for each particle using a 5th-order accurate Runge–Kutta algorithm. For each 3D simulation, 6.4×10^4 particles have been tracked (this number being reduced to 6.4×10^3 in the 2D case). Particle–domain boundary interaction has been dealt with by preventing the particles from physically penetrating the solid walls, i.e., by setting their radius as the minimal "allowed" distance from the wall itself. As already explained at the beginning of Sec. II C, since the implemented approach corresponds to a one-way coupling philosophy, this means that the relatively high number of particles used to produce the results reported in Sec. IV only served to reveal the intricate details of the particle attractors, the effective number of particles being irrelevant in terms on the emerging dynamics.

B. Validation

The algorithm described in Secs. II B, II C, and III A has already been validated extensively in earlier works of the present authors for various vibrational conditions, particle properties, and even for both the 1-way and 2-way levels of coupling (see, e.g., Crewdson and Lappa[44] and Lappa,[39] respectively).

An additional level of validation for the new thermal configuration with central thermal spots embedded into larger spots of opposite sign can be found in Ref. 32. As in the present study we consider
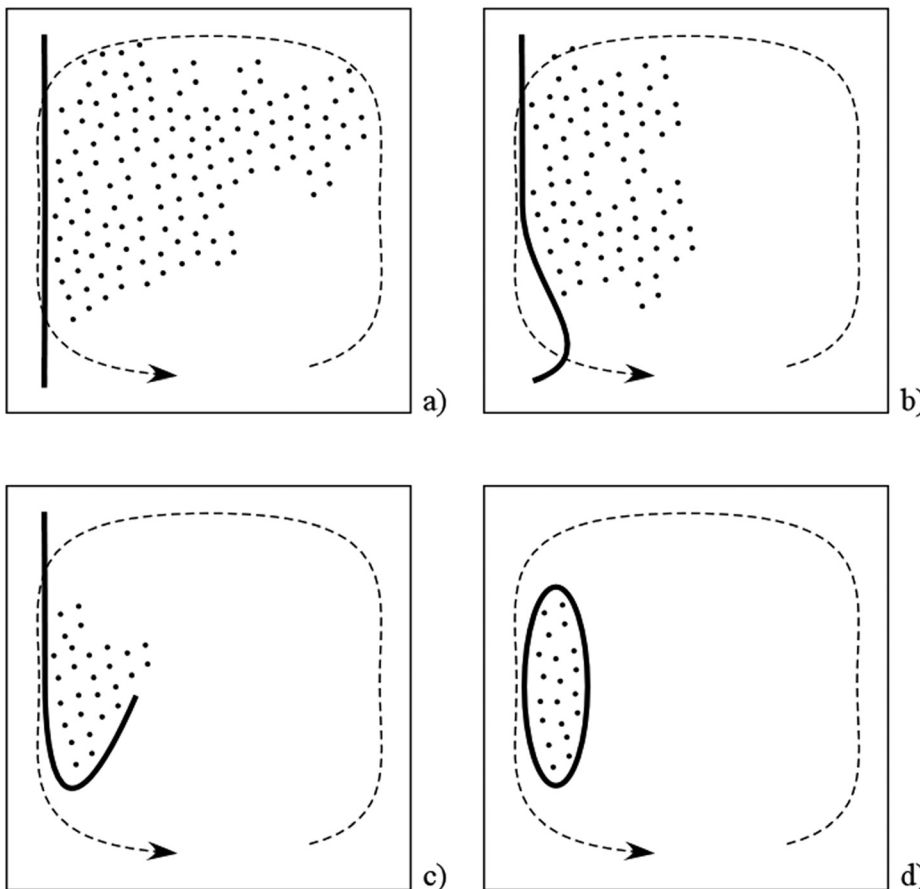

FIG. 9. Sketch of the mechanism leading to standard particle-dense boundary structures (thick solid line—particle clustering driven by cyclic particle–wall interaction; dashed line—concurrent thermovibrational flow; vibrations in the horizontal direction, temperature gradient in the perpendicular direction).

slightly different values of the governing parameters, a further level of validation has been implemented accordingly through comparison of the present computations with those obtained using the well-known OpenFOAM platform. The representative two-dimensional (2D) case ($\gamma = 10^8$, with a spot size $l_s = 0.5$) shown in Fig. 2 has been considered. Excellent agreement has been found. The snapshots were taken at a $\cong 6.55$ non-dimensional time in both cases.

IV. RESULTS

As a natural continuation of the earlier investigation by Crewdson et al.,[32] here we concentrate on a similar Prandtl number ($Pr = 6.1$ corresponding to pure water). While the main motivation of previous studies[27–30] was a definition of the precise set of parameters for an experiment to be executed on board the International Space Station,[31] the present analysis is driven by a different need, that is, the intention to collect data for the future development of an algorithm of artificial intelligence able to determine (as an output) the thermal boundary conditions required to produce particle accumulations with a desired shape or morphology (input conditions). For this reason, here the selection of the non-dimensional parameters has not been based on the specifics of the experiment hardware available on board the International Space Station;[31] rather, such characteristic numbers have been selected in order to minimize the otherwise prohibitive computational times required by the 3D numerical simulations. In this regard, we wish to recall that a formula for the determination of the time required for structure formation was originally obtained by Lappa and Burel,[30] who could successfully condense all the dependences revealed by the available numerical simulations into a single analytical expression. Since, as shown by such formula, the structure formation time grows quadratically with Ω, in the present study a relatively small value of the angular frequency is considered (i.e., $\Omega = 10^3$), while retaining values of γ, Ra_ω, and St comparable to those attained during the space experiment [$\gamma = O(10^8)$, $Ra_\omega = 10^4$, $St = 5 \times 10^{-6}$, respectively, in conjunction with a particle-to-liquid density ratio $\xi = 2$]. We wish also to highlight that another difference with respect to the work by Crewdson et al.[32] is represented by the two orders of magnitude smaller value examined in that study, i.e., $\gamma = O(10^6)$.

All cases have been initialized with a uniform distribution of particles. Following a common practice in the literature, 2D simulations have initially been used in this work as a testbed to determine the most relevant sub-range of the space of parameters to be examined. In other words, the conditions for which interesting and novel processes show up in the physical space have initially been explored under the constraint of two-dimensionality. The advantages associated with such a practice obviously stem from the reduced computational time that 2D computations require in comparison to the equivalent 3D ones. These initial simulations also serve another intentional objective or scope, that is, allowing (at a later stage) meaningful exploration of purely 3D effects through comparison with the simplified case where any processes that depend on the details of the third direction are excluded.

A. New findings under the constraint of two-dimensionality

A first sub-set of two-dimensional numerical findings are presented in Fig. 3 for the configuration in which vibrations are parallel to the y axis (i.e., $\phi = 0$, as in Crewdson et al.[32]). This initial choice obviously originates from the twofold intention to bridge the gap with that

earlier work and recall the main properties of the simplified case where the temperature gradient along the x axis undergoes two inversions only along the perpendicular direction y. As an add-on to the previous numerical study, however, the size l_s of the central spot is allowed to
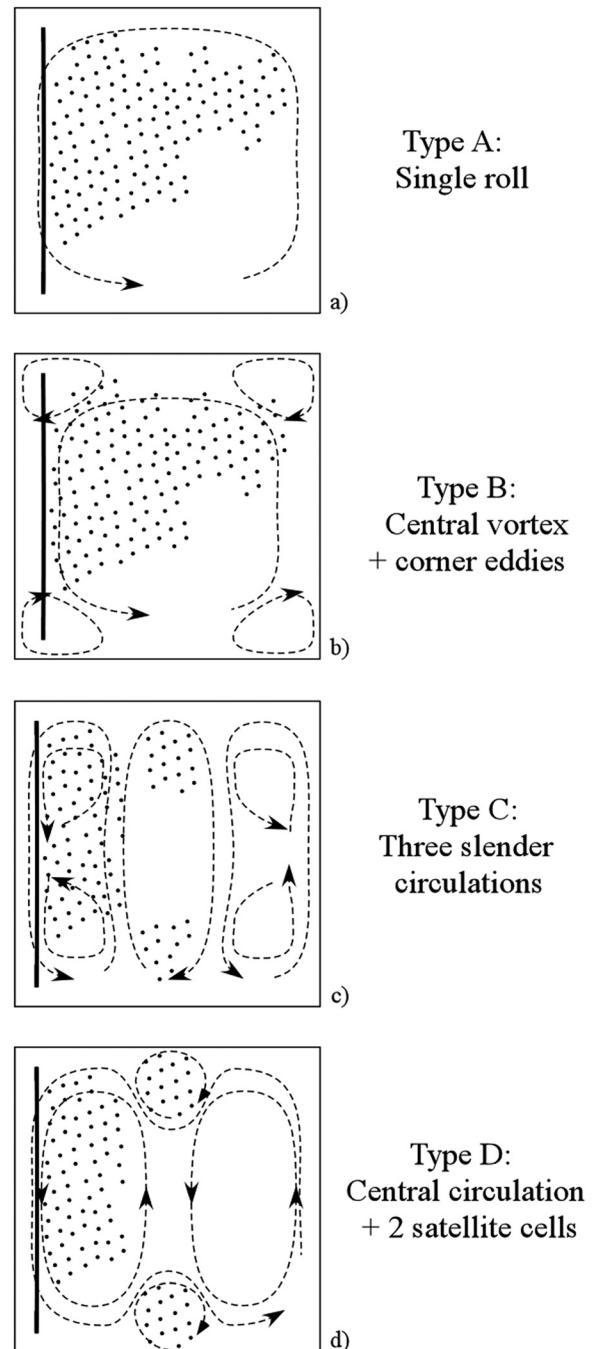

FIG. 10. Sketch of the different convective patterns produced in 2D in the $l_s = 0.2$ case (related numerical results are shown in Fig. 8): (a) Single roll, (b) central vortex + corner eddies, (c) three slender circulations, (d) central circulations + 2 satellite cells.

12 October 2023 08:29:15

span the interval $0.1 \leq l_s \leq 0.9$ (the case with $l_s = 0$ or 1 obviously correspond to the limiting condition in which uniform thermal boundary conditions are recovered).

Before starting to deal with a detailed descriptions of these results, we wish to recall briefly that a transient time exists during which the structures evolve in terms of shape and size. With time, the spatial extension of the formations tends to become smaller, thereby making them more compact and evident with respect to the "white" background (the clear fluid that is progressively depleted of particles as these converge toward the attractors). After this transient time, however, the structures attain a stable configuration in terms of size, multiplicity, and morphology. However, they do not occupy a fixed position in space; rather, the overall pattern undergoes a continuous back and forth displacement along the direction of imposed vibrations. All the snapshots reported hereafter (including those reported in Sec. IV B) relate to the situation in which the formations have attained the above-mentioned stable (asymptotic) configuration.

1. Classical and new-type particle structures

Along these lines, a first key observation stemming from Fig. 3 concerns the increase in the multiplicity N of the attracting loci (generally limited to N = 2 when uniformly heated walls are considered). Indeed, by visual inspection of this figure, the reader will immediately realize that, although in the majority of situations [Figs. 3(d)–3(g)] N

is still equal to two, specific circumstances also exist for which this parameter is doubled [as an example, N = 4 in Figs. 3(a) and 3(b)].

Additional insight follows naturally from a comparison of the boundary of the particle structures in these two panels. Most interestingly, while the left and right formations are separated from the external clear fluid by *a particle-dense boundary* (appearing as a continuous solid line in these figures, whose genesis was clarified by Lappa[27]), the other two accumulation regions do not display this feature; i.e., no marked line encapsulating the particle-rich region can be seen. Hereafter, for simplicity, these alternate particle-rich areas will be simply referred to as "boundary-free structures"; we will provide an interpretation for this notable distinguishing mark (with respect to the "classical" structures with well-defined boundaries) later. In this section, first we discuss the observable trend as the size of the central temperature spot increases while keeping fixed all the other parameters.

In this regard, as witnessed by the first two panels of the sequence [the aforementioned Figs. 3(a) and 3(b)], while increasing l_s from 0.1 to 0.2 causes a shrinkage in the size of the two classical left and right structures, vice versa, the spatial extension of the two boundary-free formation grows. In particular, this realization finds its ultimate verification in the dynamics shown in Fig. 3(c), where a degenerate state (where classical structures are no longer present) is visible for $l_s = 0.4$; and one may argue that this almost pattern-less distribution of particles simply follows from the coalescence of the two spatially separated
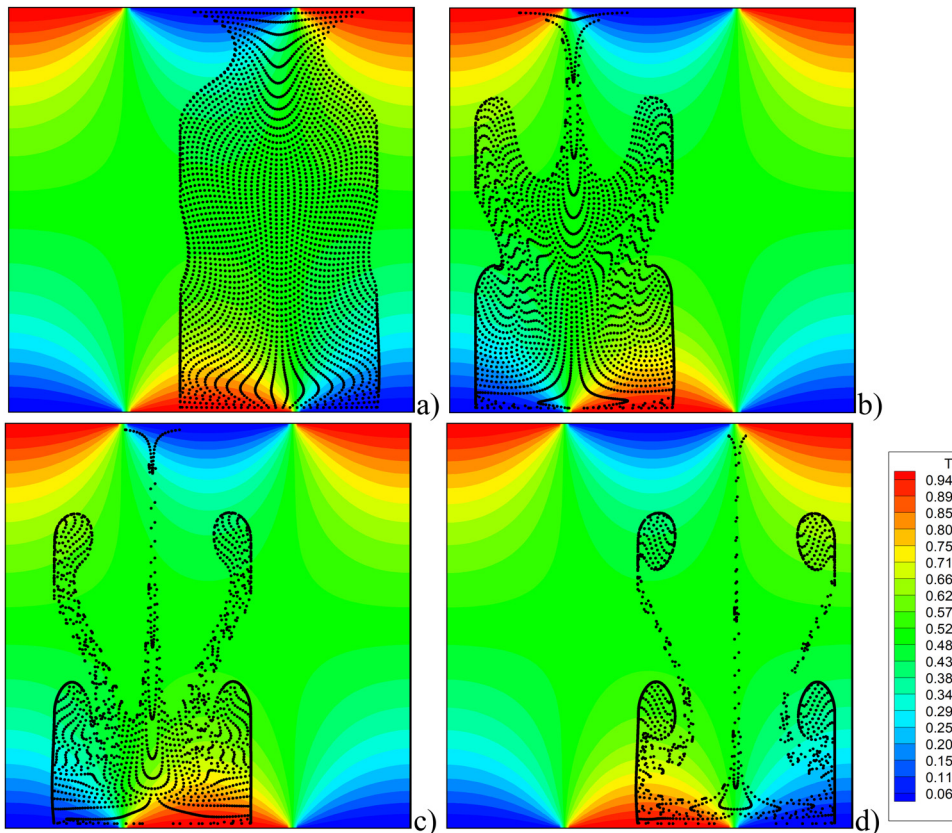

FIG. 11. Evolution in time of the particle structures for $l_s = 0.4$ and $\gamma = 3 \times 10^8$, $Ra_\omega = 10^4$, $\Omega = 10^3$, $St = 5 \times 10^{-6}$ and $\xi = 2$: (a) $t \cong 0.13$, (b) $t \cong 0.39$, (c) $t \cong 0.65$, (d) $t \cong 0.9$.

boundary-free formations that, for smaller values l_s, were protruding into the liquid from the top and bottom wall, respectively.

The next panel of the sequence [Fig. 3(d)] is also instructive. It reveals that, on further increasing l_s, the system returns to the two classical ovoidally shaped accumulations. However, these manifest themselves with a size much higher than that seen in Figs. 3(a) and 3(b). Figure 3(d) is naturally complemented by Figs. 3(e)–3(g), whose significance essentially resides in the evidence provided about the ability of the system to recover a trend where the structures undergo a size reduction as l_s is made higher.

Moving on to a case with a larger non-dimensional acceleration amplitude (see Fig. 4 for $\gamma = 2 \times 10^8$), such a variation has essentially a twofold effect. Indeed, it leads to a decrease in the size of the particle formations regardless of their nature (in order to verify this effect, the reader is encouraged to compare the different panels of Figs. 3 and 4, frame by frame); furthermore, the sequence of textural transitions

discussed for Fig. 3 is shifted to the left, i.e., the two classical left and right structures, which for $\gamma = 10^8$ were recovered for $l_s = 0.5$, reenter the dynamics for a relatively smaller value of l_s in the $\gamma = 2 \times 10^8$ case [i.e., $l_s = 0.4$ in Fig. 4(c)].

These trends are confirmed by the additional data collected in Fig. 5. This figure also provides a glimpse of the more complex dynamics that are enabled when specific combinations of γ, St, and ξ are considered [with Fig. 5(b) representing, in particular, the "four-loop" structure type already reported by Crewdson et al.[32]).

2. Ensemble dynamics and size trends

The reader will get a better impression or realization of the "ensemble" dynamics of this system by taking a look at the additional plots shown in Figs. 6 and 7 (where the system behaviors have been
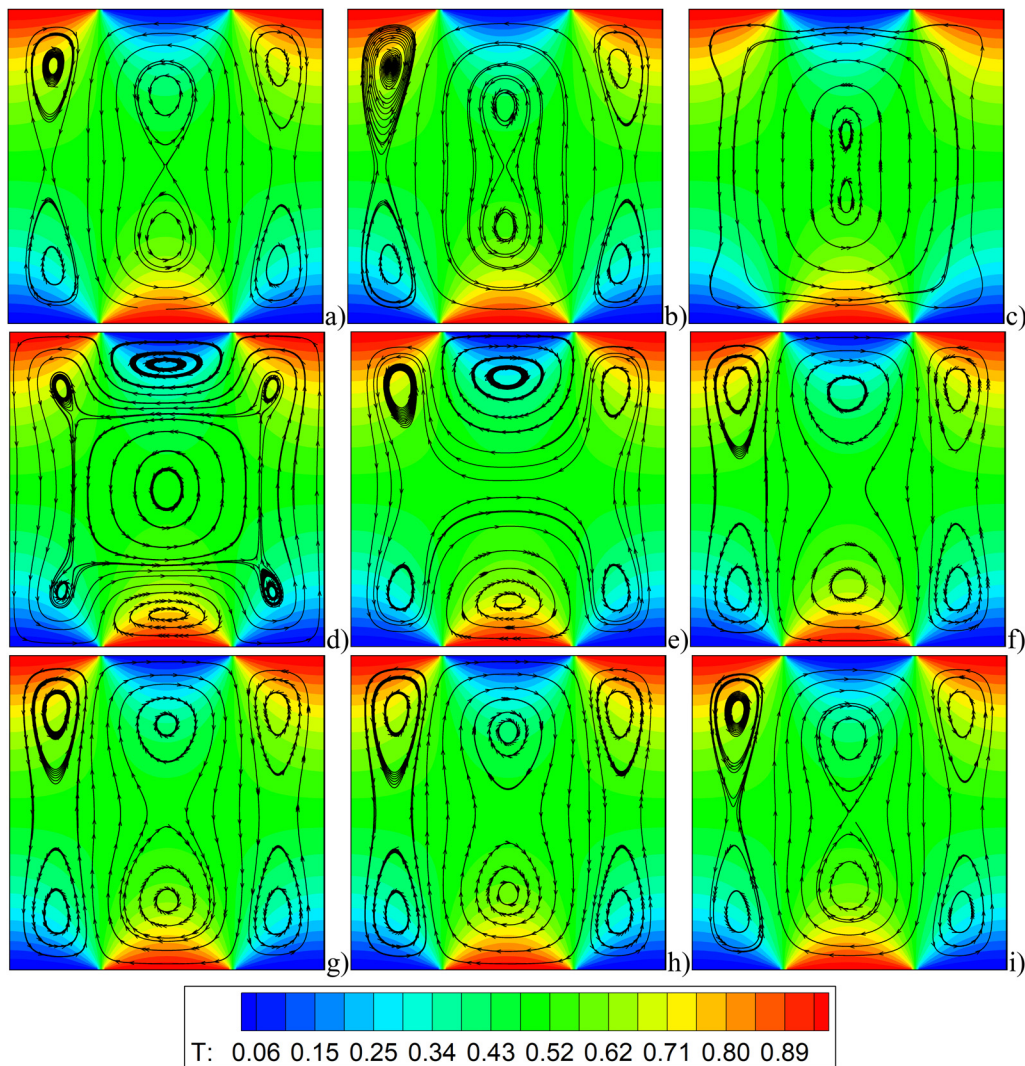

FIG. 12. Nine snapshots of temperature and streamlines evenly spaced within half of the forcing period $P = 2\pi/\Omega$ for $Ra_\omega = 10^4$, $\Omega = 10^3$, and $l_s = 0.4$ (2D computations).
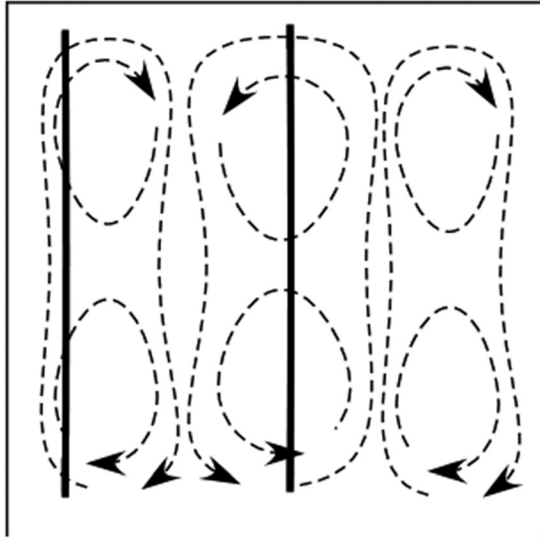
FIG. 13. Sketch of the mechanism leading to four standard particle-dense boundary structures (vibrations in the horizontal direction).

summarized by means of branches accounting separately for the evolution of the different structure types describe before).

The piecewise nature of these plots, i.e., the related "discontinuities" and their alternating slopes, i.e., the different trends that formations of different types display in terms of related sensitivity or dependence on the spot size (l_s), should be regarded as clues or hints for the different patterning processes at work. While in many cases, such mechanisms exclude each other, in other cases coexistence is allowed (although this happens only in limited subranges of l_s, i.e., 0.1 $\leq l_s \leq 0.3$ for $\gamma = 10^8$ and $l_s = 0.1$ only for $\gamma = 2 \times 10^8$).

As already discussed to a certain extent in the preceding text, an increase in γ (see Fig. 7), generally, causes the downward displacement of the branches related to standard structures and/or a shrinkage (or complete suppression) of the intervals where the boundary-free formations are allowed.

3. Underlying mechanisms

Given the "diverse" behavior of these alternate structures, we intentionally use the remainder of this section to clarify the underlying cause-and-effect relationships. In order to do so, in particular, we start from the simple remark that an explanation for them has (obviously) to be sought in the hybrid thermovibrational–inertial nature of the
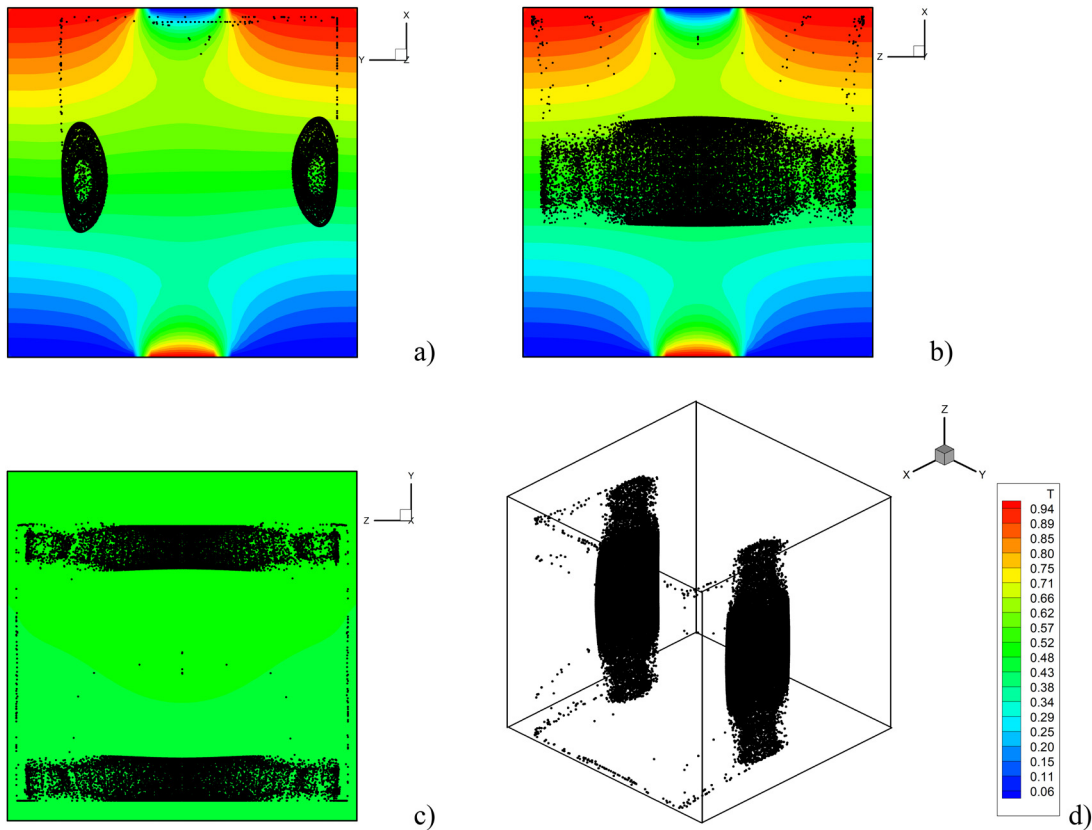

FIG. 14. Snapshot (3D views for $t \cong 8.96$) of particle structures and related temperature distribution for $\gamma = 10^8$, $Ra_\omega = 10^4$, $\Omega = 10^3$, $St = 5 \times 10^{-6}$, $\xi = 2$, $\phi = 0°$, and $l_s = 0.2$: (a) perspective perpendicular to the xy mid-plane, (b) perspective perpendicular to the xz mid-plane, (c) perspective perpendicular to the yz plane, (d) isometric 3D view.

considered phenomena. Along these lines, an approach similar to that implemented by Lappa[27] to elucidate the genesis of the classical (boundary-dense) structures is therefore used. Put simply, we consider the different stages of evolution taken by the flow in conjunction with its effect on the particle distribution (the reader being referred to Fig. 8 for the related sequence of snapshots over half of the period of forcing in the $l_s = 0.2$ case). Direct comparison with the arguments provided in the earlier work[27] for the situation with unidirectional temperature gradient is also useful in this regard. Indeed, it is worth recalling that when uniform heating is considered, the formation of the "classical" structures can be ascribed to the ability of particles to periodically hit the walls perpendicular to vibrations as a result of their sensitivity to the acceleration induced by vibrations (independently from any fluid-dynamic effect) and the ensuing ability of thermovibrational convection to cause *the folding* of the (otherwise straight and parallel to the walls) "particle accumulation lines" formed due to such collisions.

Although a detailed description of this process has already been reported in that work, for the convenience of the reader, its salient aspects are also sketched here in Fig. 9, where the tick solid line is used to indicate the particle clustering effect driven by the particle–wall interaction, while the dashed line depicts the concurrent thermovibrational flow.

When uniform heating/cooling is applied, the latter consists of a single vortex (pervasive throughout the cavity), which changes continuously its sense of rotation (from clockwise to counterclockwise) and is able to transport alternatively all the particles located in the bulk toward the lateral accumulation lines. In particular, for simplicity, the sketch shows only the morphological changes undergone by the particle-dense line located in proximity to the left (adiabatic) wall of the cavity as a result of its interaction with the thermovibrational roll when it is oriented in the counterclockwise direction (analogous arguments hold for the evolution of the accumulation line located near the right sidewall due to its interaction with the rolls when it is oriented in the clockwise direction).

As qualitatively substantiated by this figure, four main stages can be recognized in this process. The formation of the bulge in the lower half of the cavity [Fig. 9(b)] is due to the rightward drag that the flow exerts on the particles previously collapsed on a single line owing to the force pushing them toward the left wall. As the particle-dense line detaches from the wall (as soon as the vibrationally induced acceleration changes its sign, i.e., particles are pushed inward), this line is distorted due to a purely fluid-dynamic effect. The reason why as similar bulge is not created in the upper part of the cavity is due to the fact that the drag effect and the body force have opposite signs in that region and tend to compensate each other (which explains why the
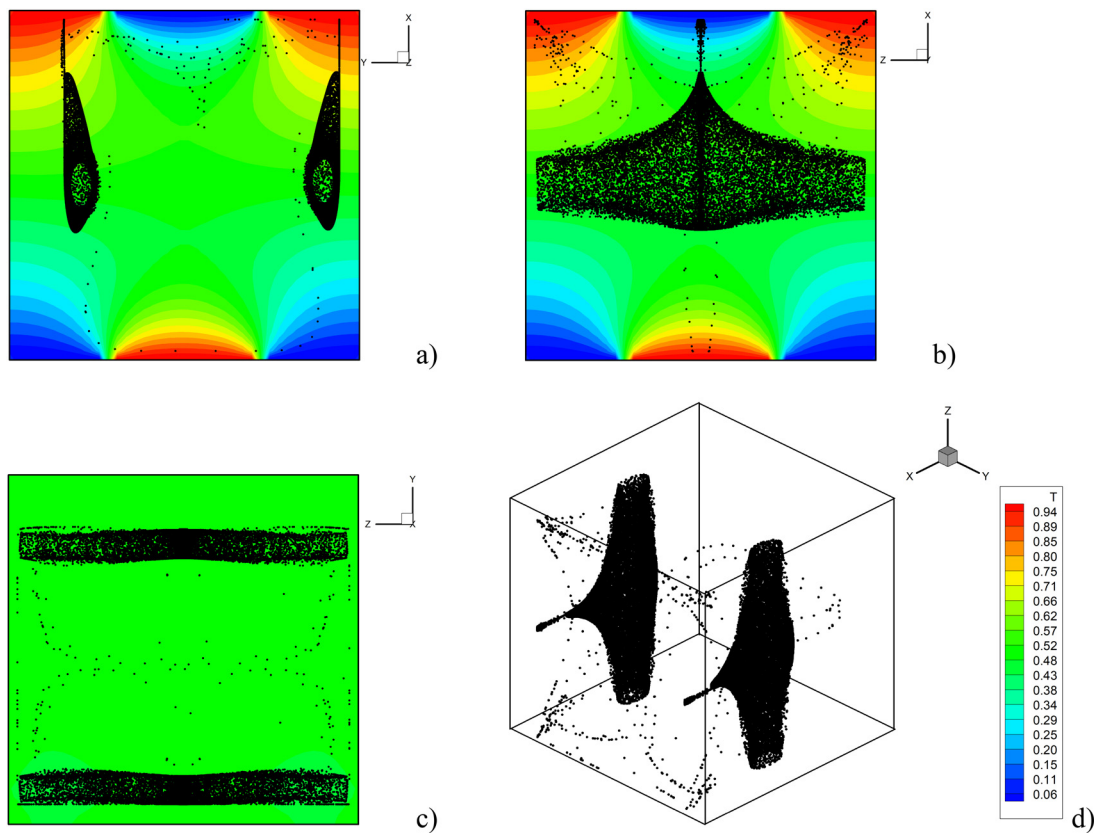

FIG. 15. Snapshot (3D views for $t \cong 8.96$) of particle structures and related temperature distribution for $\gamma = 10^8$, $Ra_\omega = 10^4$, $\Omega = 10^3$, $St = 5 \times 10^{-6}$, $\xi = 2$, $\phi = 0°$, and $l_s = 0.4$: (a) perspective perpendicular to the xy mid-plane, (b) perspective perpendicular to the xz mid-plane, (c) perspective perpendicular to the yz plane, (d) isometric 3D view.

process is not symmetric with respect to the x = 0.5 mid-plane of the cavity). These processes are iterated until a closed line (a particle loop or circuit) is obtained, which serves as a boundary encapsulating the particle attractee[27] [Fig. 9(d)].

As witnessed by the existence of structures with a well-defined boundary, a similar mechanism is obviously still effective in the case where the temperature along the thermally active walls is not uniform (present study). In particular, an explanation/justification for the emergence of structures with a particle-dense boundary can be elaborated in its simplest form on the basis of the argument that long subranges of the oscillation period exist, where the flow still corresponds to a single vortex extended throughout the cavity rotating in the clockwise or counterclockwise direction [see Figs. 8(a)–8(c) and 8(g)–8(i), respectively]; in some subranges of the forcing period, a central larger vortex with four small eddies located in the cavity corners is formed [Fig. 8(d)], which is also able to fold the otherwise straight lateral accumulation lines.

These situations have been sketched in Fig. 10. Cases exist where the aforementioned single roll [Figs. 8(a)–8(c) and 10(a)] is surrounded by other small vortices located in the corners of the cavity [situation sketched in Fig. 10(b) and visible in Fig. 8(d)] or it is broken into three independent circulations [sketched in Fig. 10(c) and visible in Fig. 8(e)] or two main vortices are present in the bulk (located in the left and right portions of the cavity, respectively), embedded in a larger

circulation with two localized minor vortices occupying the central top and bottom regions adjacent the thermal spots [sketched in Fig. 10(d) and visible in Figs. 8(f), 8(g) and 8(h)]. For convenience, hereafter, these four configurations of the convective pattern are simply referred to as "single-roll," "central vortex + corner eddies," "three-slender-circulations," and "central circulation + 2 satellite cells" states, respectively (or, more conveniently, simply as "type A," "type B," "type C," and "type D" patterns).

While particle interaction with the type A or B patterns would obviously lead to dynamics similar to that produced in the classical case with uniform heating, obviously, a separate discussion is needed for the other two cases.

The dispersed solid mass affected by the central circulation typical of the type C pattern [Fig. 10(c)] or located in the regions corresponding to the two small satellite vortices of the pattern D [Fig. 10(d)] will clearly be prevented from reaching the lateral regions, where they might hit the wall and be accumulated into the classical structures. Owing to the alternation in time of convective patterns with different topologies, there will be some particles that tend to remain in the central area simply because the time they are exposed to the single pervasive roll (pattern A or B) is not enough to let them leave that region before they are captured by circulations of the C or D types. Furthermore, evidence corroborating this interpretation stems from the lack of particle-dense boundaries in these alternate
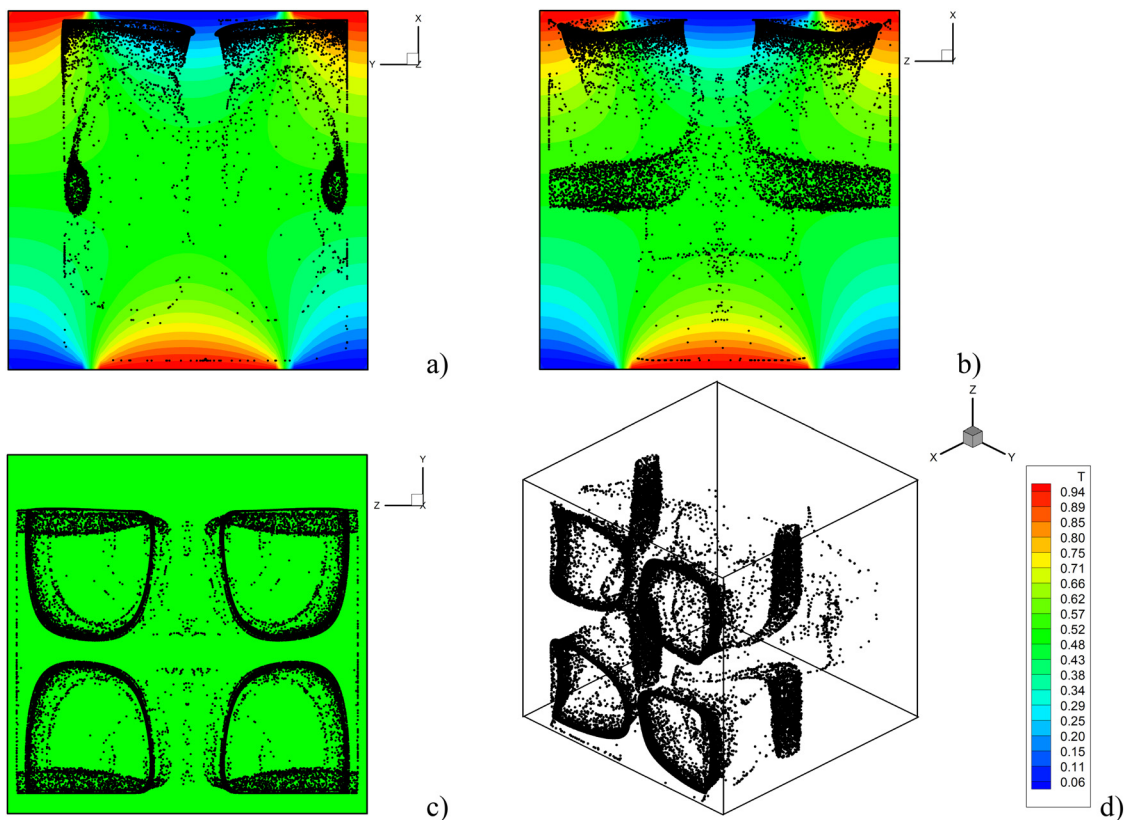

FIG. 16. Snapshot (3D views for $t \cong 8.96$) of particle structures and related temperature distribution for $\gamma = 10^8$, $Ra_\omega = 10^4$, $\Omega = 10^3$, $St = 5 \times 10^{-6}$, $\xi = 2$, $\phi = 0°$, and $l_s = 0.5$: (a) perspective perpendicular to the xy mid-plane, (b) perspective perpendicular to the xz mid-plane, (c) perspective perpendicular to the yz plane, (d) isometric 3D view.

accumulation regions, which clearly indicates that the particles in these regions *never hit the lateral walls*, i.e., the boundaries perpendicular to the imposed vibrations.

As indirectly confirmed by Figs. 3 and 4 (for $\gamma = 10^8$ and $\gamma = 2 \times 10^8$, respectively), and a representative value of the vibrational Rayleigh number ($Ra_\omega = 10^4$), this phenomenon is allowed only in specific ranges of the parameters l_s and γ, the former being responsible for the effective existence of transitional stages of evolution of the C and D types show in Fig. 10 (which are generally suppressed in the limit as l_s tends to either 0 or 1), the latter accounting for the magnitude of the body force that vibrations exert on particles (pushing them toward the sidewalls).

A separate discussion is needed for the $\gamma = 3 \times 10^8$ case, this being the only situations for which 4 standard structures are obtained (also requiring a relevant explanation).

The related stages of evolution of the particle distribution as time passes have been summarized in Fig. 11. These make immediately evident that the initial amphora-like shape of the pattern [Fig. 11(a)], produced by the interaction of the side particle-dense lines with the main convective circulation [refer again to the mechanism illustrated in Fig. 9 and, in particular, to Fig. 9(b)], is much more compressed along the direction of vibrations than in other cases (its size along the y axis is relatively small in comparison to the

other cases with smaller γ, it being even shorter than half of the cavity extension). This is obviously due to the relatively high values of γ (3×10^8), which is also responsible for the larger horizontal displacements undergone by the particles (the corresponding structure indeed continuously moves from the very left to the very right side and vice versa). Analysis of the textural transition undergone by the velocity field (Fig. 12), however, reveals that the higher value of γ is not the only factor contributing to the emergence of four independent boundary-dense structures. It can be seen that for the specific case $l_s = 0.4$, convective circulations of the C type are dominant.

While this feature still leads to the classical two structures for $\gamma = 2 \times 10^8$, for $\gamma = 3 \times 10^8$, it causes a significant departure from this condition as, given its reduced extension along the y axis, both particle-dense lateral lines separating the structure from the clear fluid outside can interact alternatively with the left and central circulations or with the central and right ones. Each of these in turn encapsulates two co-rotating rolls, which can cause a similar deformation of these lines at two different stations along x (Fig. 13), thereby, supporting (as these effects accumulate in time) the formation of four independent particle circuits. Obviously, like the $\gamma = 2 \times 10^8$ case, particle-free regions are not allowed for $\gamma = 3 \times 10^8$ as all the particles can periodically hit the sidewalls.
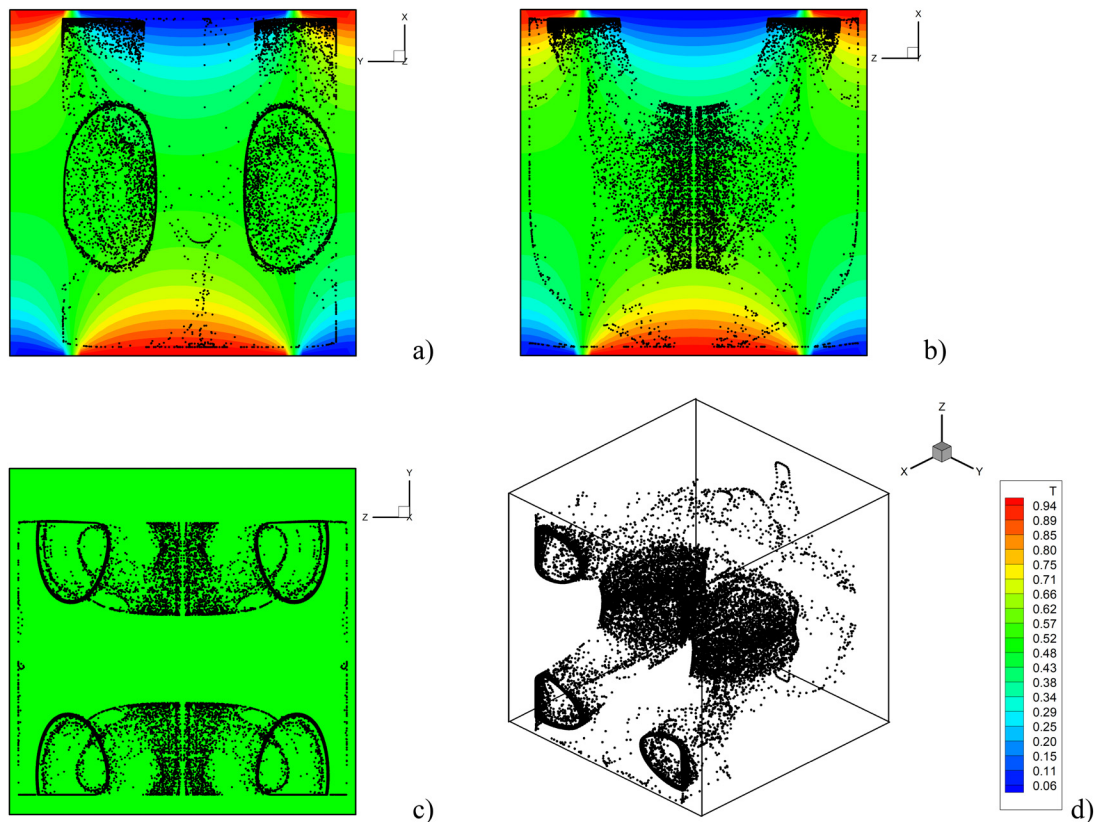

FIG. 17. Snapshot (3D views for $t \cong 8.96$) of particle structures and related temperature distribution for $\gamma = 10^8$, $Ra_\omega = 10^4$, $\Omega = 10^3$, $St = 5 \times 10^{-6}$, $\xi = 2$, $\phi = 0°$, and $l_s = 0.6$: (a) perspective perpendicular to the xy mid-plane, (b) perspective perpendicular to the xz mid-plane, (c) perspective perpendicular to the yz plane, (d) isometric 3D view.

B. 3D simulations and resulting pattern formation

1. Area ratio effects

Given the absence of "*a priori* available" data to properly constrain the model parameters in the 3D case, as already discussed to a certain extent in the earlier text, the preliminary information obtained in the framework of 2D simulations has been used in this study as a basis (or as a "forecast criterion") to select an initial set of promising 3D cases to be simulated. In order to do so, in particular, we have initially exploited a couple of somehow "heuristic principles," and that is, a 3D case is defined in such a way that: (1) its l_s is exactly the same as that considered in 2D or (2) *the ratio of the central spot area and the area of the wall* are (approximately) the same. As these ratios read l_s and $(l_s)^2$ in 2D and 3D, respectively, this means that, in the latter situation, a 3D case "equivalent" to the 2D one with a given $(l_s)_{2D}$ would correspond to a $(l_s)_{3D} \cong \sqrt{(l_s)_{2D}}$.

Following up on the previous point, Fig. 14 provides a first glimpse of the dynamics enabled in 3D for $\gamma = 10^8$, $l_s = 0.2$, and $\phi = 0$. This figure is instrumental in showing that the two particle structures formed in the bulk of the liquid essentially resemble those already observed in 2D, namely, a couple of ellipsoidally shaped accumulations in the xy plane [Fig. 14(a)]. The almost constant cross-sectional area along most of the z extension of the computational domain [see Figs. 14(b) and 14(c)] confirms their essentially two-dimensional nature.

The next figure of the sequence (Fig. 15), however, also leads to valuable insight. Indeed, it illustrates that the changes induced in the pattern by an increase in l_s from 0.2 to 0.4 are not as significant as one would expect on the basis of earlier/available 2D results (Fig. 3 in Sec. IV A); the most important outcome of this observation is that the application of the aforementioned "same-l_s," criterion should not be seen as an effective way to interpret the dynamics.

In the 3D case, on doubling the linear size of the thermal patch, the only visible modifications affect the morphology of the structures in the xy plane. The two ellipsoids seen for $l_s = 0.2$ are taken over for $l_s = 0.4$ by two elongated drop-shaped structures with comparable transverse size (along y).

In qualitative agreement with the 2D findings, however, a further increase in l_s (=0.5 in Fig. 16) causes a shrinkage in the size of such formations (thereby lending more credibility to the aforementioned $(l_s)_{3D} \cong \sqrt{(l_s)_{2D}}$ equivalence criterion for which the phenomena in 3D should be somehow similar to those occurring in 2D for $(l_s)_{2D} = [(l_s)_{3D}]^2 = 0.25$). The 3D circumstances with $l_s = 0.5$ deserve special attention also because the two aforementioned structures are not the only recognizable formations. An observer taking a look at the physical domain from a perspective perpendicular to the yz plane, indeed, would easily recognize a sort of "quadrupolar" pattern in proximity to the x = 1 plane (top wall corresponding to panel c in Fig. 16), consisting of four independent tubular "circuits" or "loops" having diameter comparable to half of the cavity size L and a relatively limited extension along x.

2. Quadrupolar patterns

The specific feature revealed by Fig. 16 has never been reported in earlier 3D investigations on the subject. In particular, two remarkable characteristics stand out from it and need to be pinpointed suitably here. In addition to the aforementioned four cylindrically shaped particle accumulation surfaces located near the x = 1 plane (with axes

perpendicular to such a plane), the two "classical" ellipsoidally shaped structures with axes parallel to the z direction (as seen through the lateral xy plane) display a kind of discontinuity or breakage effect just in the center. Remarkably, due to this behavior, the total number of distinguishable (i.e., spatially separated) formations attains a value as high as N = 8 (last panel of Fig. 16).

The quadrupolar feature is still a prominent property of the pattern if l_s is increased to 0.6. The morphological transformations undergone by the particle formations still deserve discussion in this case. In fact, the evolution is not trivial and leads to another possible realization in terms of structure multiplicity. In place of the breakage effect
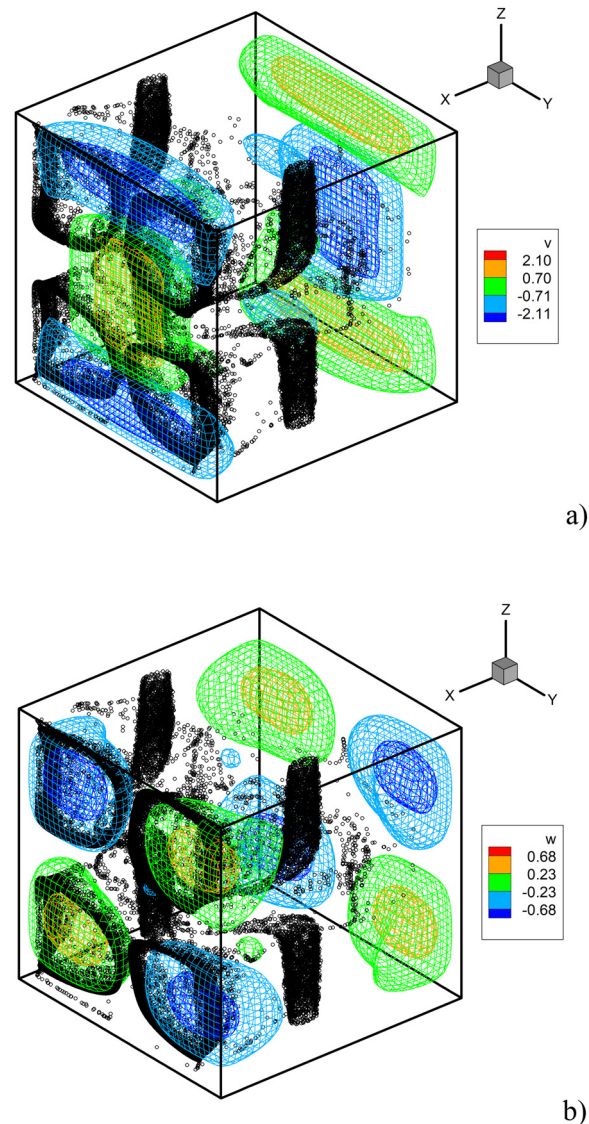

FIG. 18. Combined 3D view showing particles and the instantaneous fluid velocity for the same conditions considered in Fig. 16 ($l_s = 0.5$): (a) Isosurfaces of the velocity component (v) along the direction of vibrations (y axis), (b) isosurfaces of the velocity component (w) along the spanwise z direction.
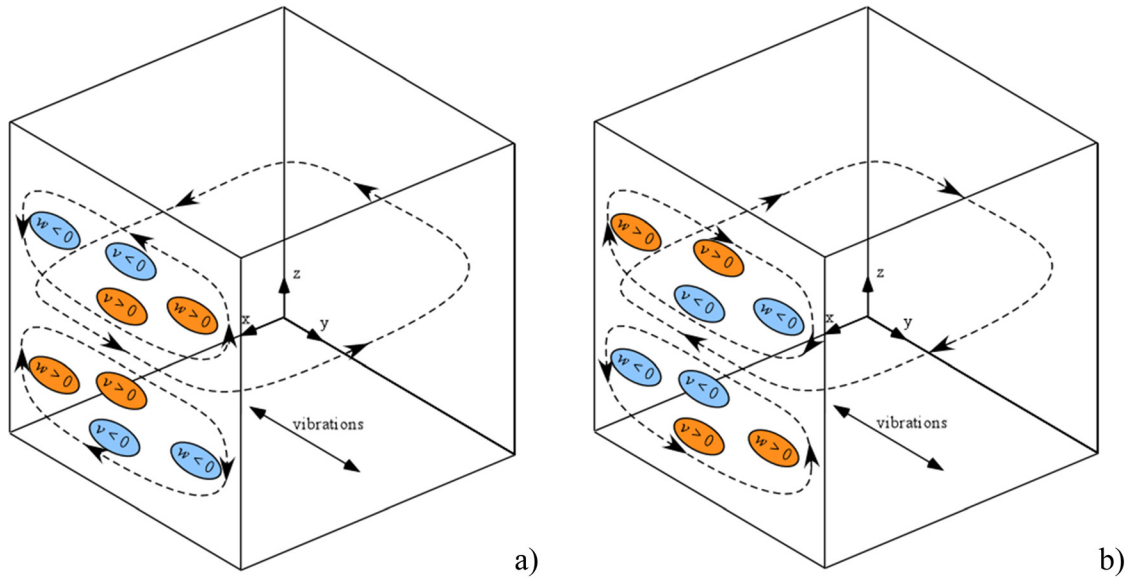
FIG. 19. Illustration of the 3D flow resulting from the combination of a main circulation in the xy plane and two additional vortices existing in a region of limited extend adjacent the x = 1 wall: (a) $t = t_o$; (b) $t = t_o + P/2$.
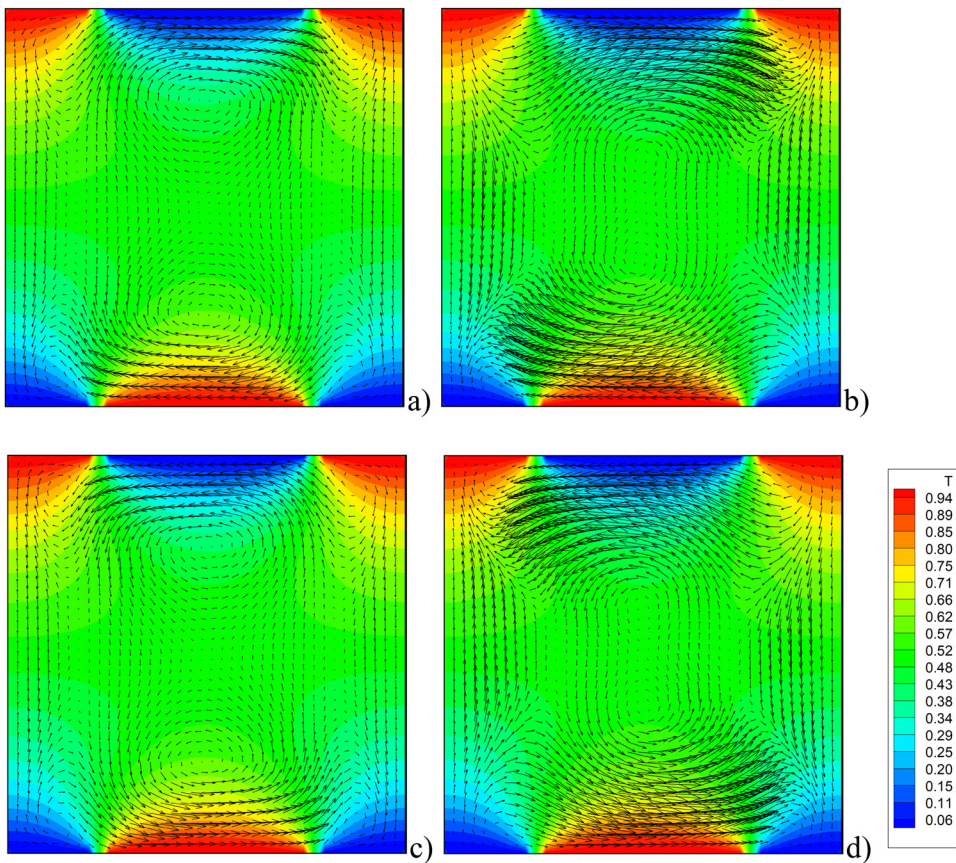

FIG. 20. Four snapshots of temperature and velocity fields evenly spaced within one complete forcing period $P = 2\pi/\Omega$ for $Ra_\omega = 10^4$, $\Omega = 10^3$, and $l_s = 0.5$ (3D computations, xy mid-plane).
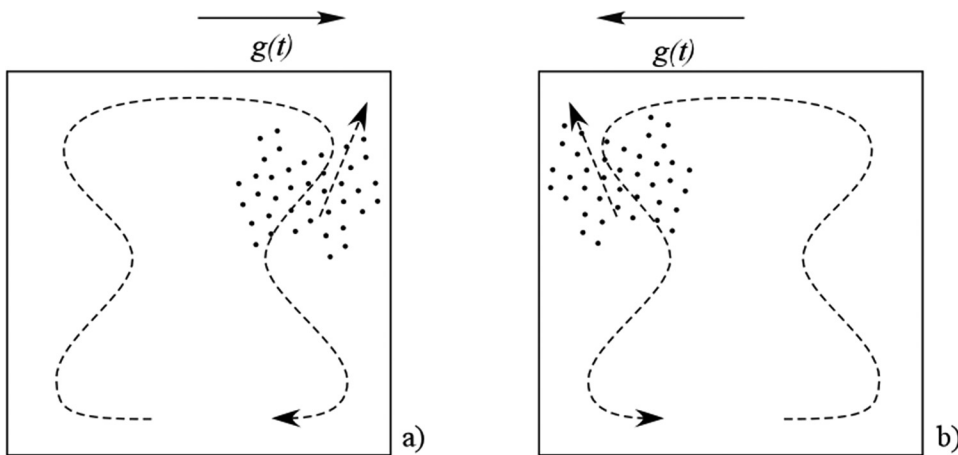
FIG. 21. Sketch showing the fluid flow direction in the xy mid-place for the conditions corresponding to Figs. 20(b) and 20(d) (the direction of the fluid current and the density-difference-driven body force indicated by dashed and solid arrows, respectively).

reported for $l_s = 0.5$, the two main structures located in the bulk of the fluid undergo a sort of compression along the spanwise direction z. Accordingly, the area of their projection in the xy plane increases significantly, and given the cohesive nature of these two central formations, the overall multiplicity of the pattern becomes N = 6 (Fig. 17).

3. Cause-and-effect relationships

Given the heretofore unseen presence of the aforementioned quadrupolar feature and the unique properties of the resulting pattern in terms of multiplicity, we open now a short excursus on the underlying mechanisms. In practice, in a similar vein to the approach already
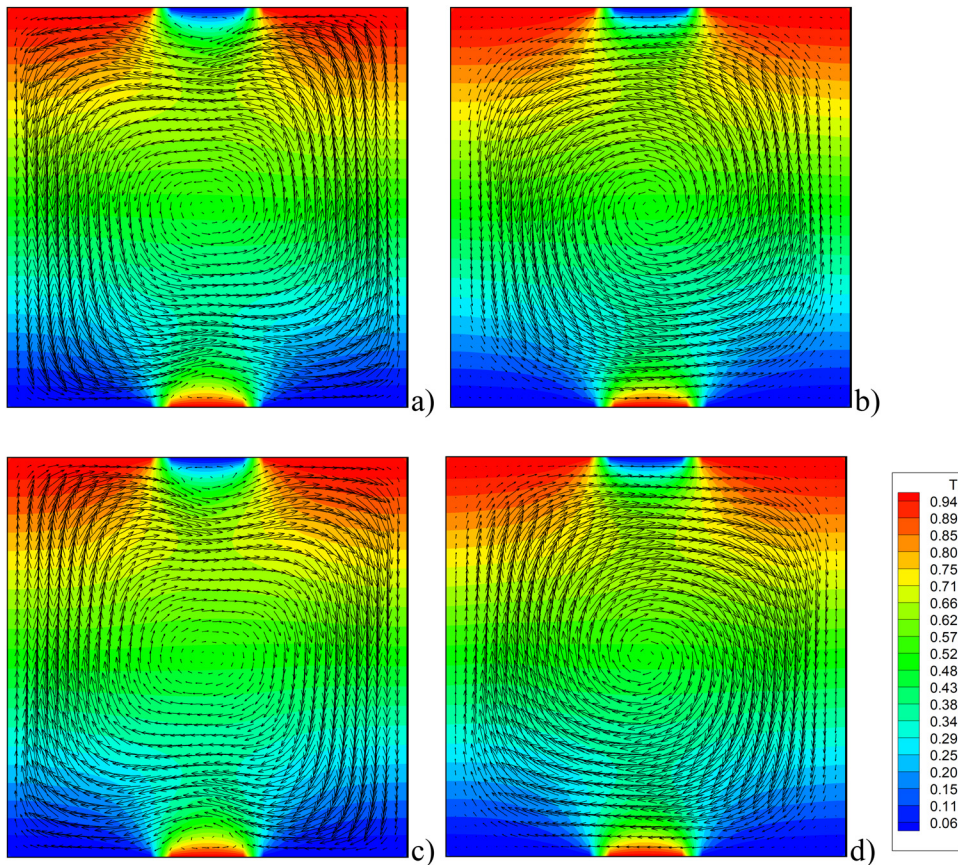

FIG. 22. Four snapshots of temperature and velocity fields evenly spaced within one complete forcing period $P = 2\pi/\Omega$ for $Ra_\omega = 10^4$, $\Omega = 10^3$ and $l_s = 0.2$ (3D computations, xy mid-plane).
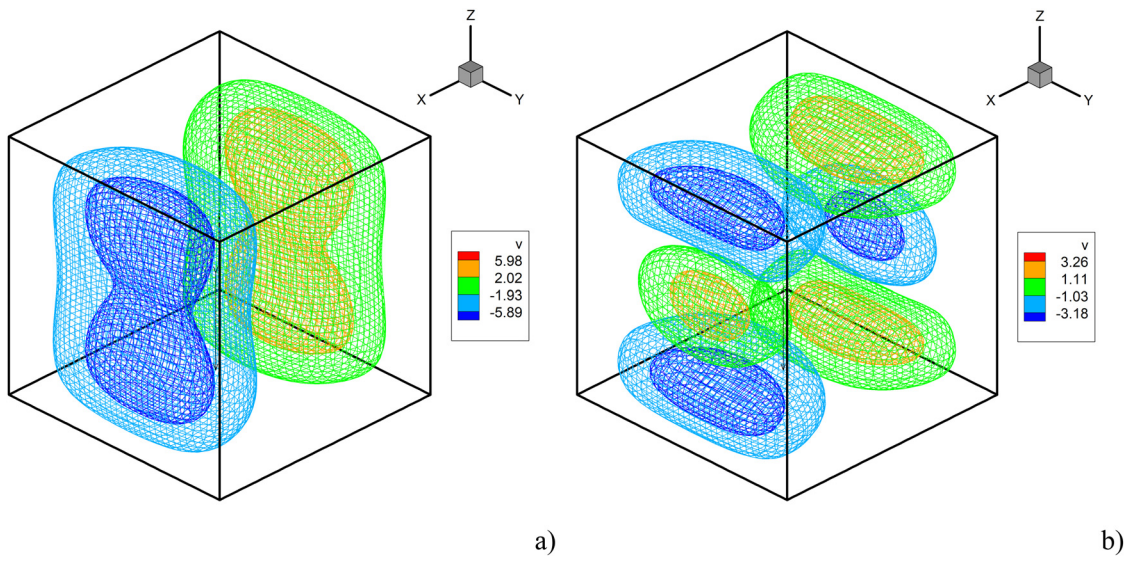
FIG. 23. Snapshots of the instantaneous fluid velocity (3D computations, isosurfaces of the component along the direction of vibrations): (a) $l_s = 0.2$ (corresponding to the same conditions considered for Fig. 22); (b) $l_s = 0.5$ (corresponding to the same conditions considered for Fig. 20).
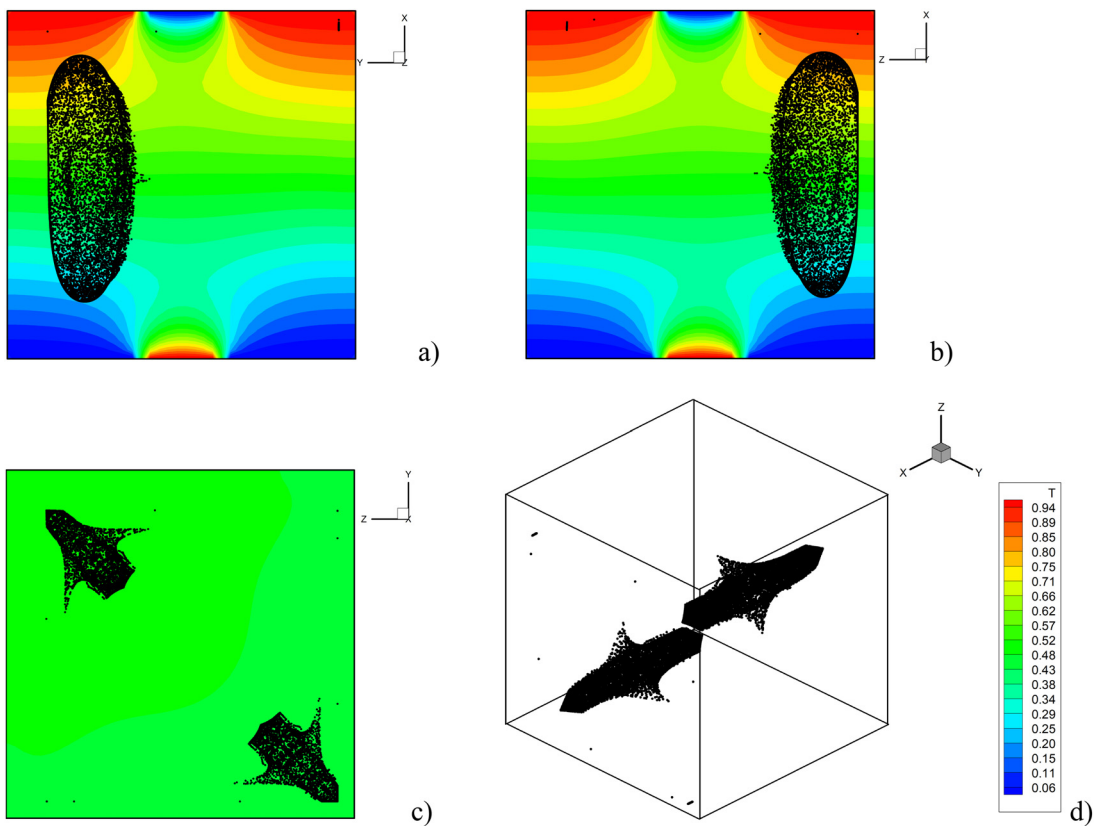

FIG. 24. Snapshot (3D views for $t \cong 8.96$) of particle structures for $\gamma = 10^8$, $Ra_\omega = 10^4$, $\Omega = 10^3$, $St = 5 \times 10^{-6}$, $\xi = 2$, $\phi = 45°$, and $l_s = 0.2$: (a) perspective perpendicular to the xy mid-plane, (b) perspective perpendicular to the xz mid-plane, (c) perspective perpendicular to the yz plane, (d) isometric 3D view.

used to interpret the formation of the classical couple of cylindrical structures with axes parallel to the z axis (the reader being referred again to Fig. 9 and related arguments in the text), this endeavor requires proper consideration of the time-varying nature of the velocity field in conjunction with the corresponding behavior of the particle structures. For simplicity, we concentrate on the same conditions considered in Fig. 16. Along these lines, a good impression of such interplay can be gathered from Fig. 18, where we have plotted the particle distribution together with the isosurfaces of the velocity components along y and z, respectively, at a given (fixed) time.

These snapshots reveal that, in proximity to the x = 1 (yz plane) wall, the convective configuration essentially consists of two rolls with limited extension along x. These two vortices change their direction periodically (from the clockwise to the counterclockwise direction and vice versa) as the main circulation visible in the xy mid-plane also does (the reader being also referred to the helpful sketch shown in Fig. 19).

One may therefore argue that, just as the main xy circulation is able to support the formation of two independent cylindrical particle structures with axes parallel to the z axis, each of the two vortices located near the x = 1 plane can produce a couple of independent formations with axes parallel to the x direction. The underlying mechanism is essentially the same illustrated schematically in Fig. 9; i.e., it relies on the ability of the vortices present in the flow to fold progressively the straight accumulation lines perpendicular to the vibration

direction (y axis in this case) where particles tend to be collected as a result of their interaction with the solid walls.

Some rationale, however, is also needed to clarify why the quadrupolar set of structures manifest itself only for some values of l_s, while the pattern reduces to the classical N = 2 configuration in other circumstances (e.g., Figure 14).

Building on the aforementioned $(l_s)_{3D} \cong \sqrt{(l_s)_{2D}}$ equivalence (in agreement with this criterion, the quadrupolar pattern shows up more or less under the same conditions for which the boundary-free formations are produced in 2D), we infer that this pattern only exists if a certain amount of particles is trapped in proximity to (or transported toward) the thermally controlled wall x = 1. This is indeed what even a fleeting look at Fig. 20 would immediately confirm. This figure contains a sequence of evenly distributed in time snapshots of the temperature and velocity fields in the xy mid-plane for $l_s = 0.5$. It makes evident that the convective circulation in this plane reduces to a relatively small roll located in the center of the cavity [Figs. 20(b) and 20(d)] over almost 50% of the forcing period.

Even more importantly, as a closer inspection of Fig. 20 would confirm, in the time intervals where the flow is reduced to a central vortex of limited extent, fluid currents exist that transport alternatively particles from the central region toward the right (left) upper corner of the cavity in such a way that they can hit the right (left) wall. These currents are indeed synchronous and concurrent with the
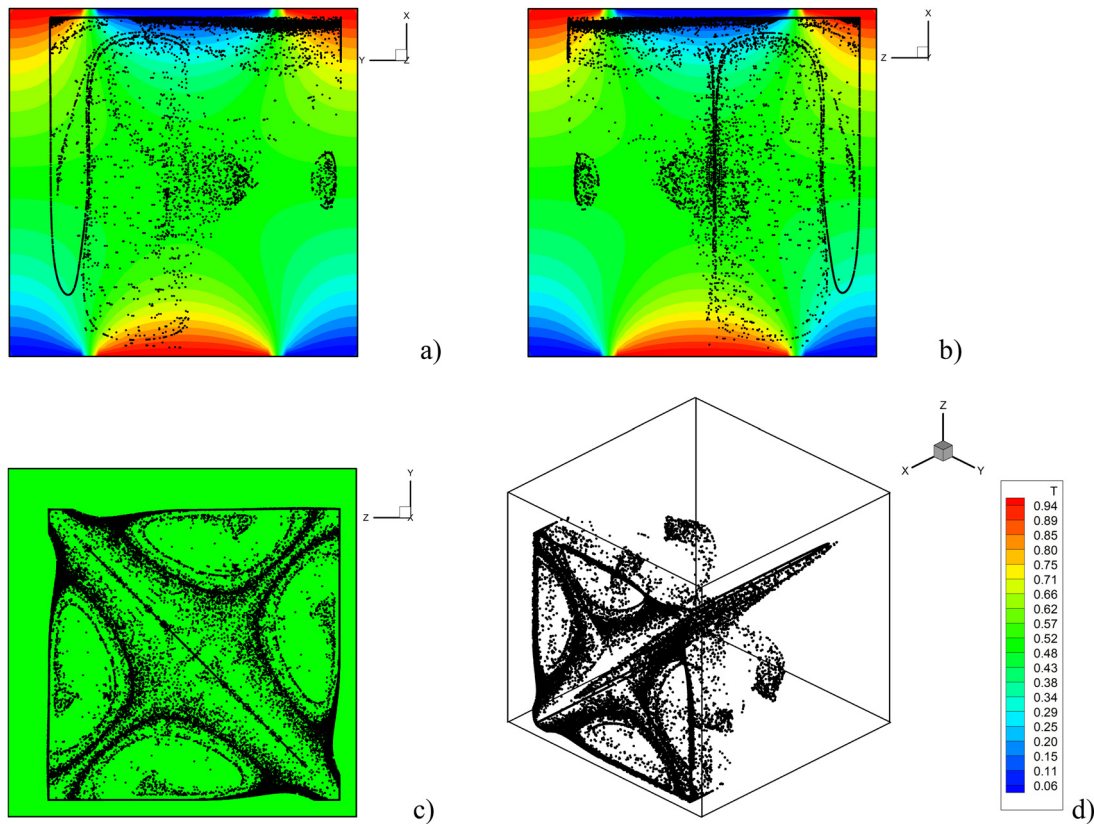

FIG. 25. Snapshot (3D views for $t \cong 8.96$) of particle structures for $\gamma = 10^8$, $Ra_\omega = 10^4$, $\Omega = 10^3$, $St = 5 \times 10^{-6}$, $\xi = 2$, $\phi = 45°$, and $l_s = 0.5$: (a) perspective perpendicular to the xy mid-plane, (b) perspective perpendicular to the xz mid-plane, (c) perspective perpendicular to the yz plane, (d) isometric 3D view.

density-difference-driven body force acting on particles. For the convenience of the reader, the related mechanism has been clearly depicted in another sketch (Fig. 21). In this sketch, the direction of the fluid current (and the corresponding drag exerted on solid particles) and the density-difference-driven body force have been indicated using dashed and solid arrows, respectively.

Comparison of Fig. 20 with the equivalent one obtained for $l_s = 0.2$ (Fig. 22) immediately reveals that this unique combination of viscous and density-driven forces acting on the particles is not attained when the configuration with a smaller extension of the spot is considered. For $l_s = 0.2$, only the classical *single roll, extended throughout the cavity* in the xy mid-plane, which changes continuously its sense of motion from the clockwise to the counterclockwise direction, can be recognized (Fig. 22).

Figure 23 complements this analysis by showing that the $l_s = 0.2$ case lacks not only the feedback mechanism illustrated in Fig. 21 but also the two convective circulations located in proximity to the x = 1 wall, required to shape the particles being accumulated in proximity to the x = 1 plane in the form of a quadrupolar pattern [compare Figs. 23(a) and 23(b) for $l_s = 0.2$ and $l_s = 0.5$, respectively; in the former case, no sign inversion can be seen in the isosurfaces of the v component in proximity to the x = 1 plane, which indicates that the two vortices sketched in Fig. 19 do not exist in this case].

4. Inclined vibrations

Having completed a description of the dynamics shown in Figs. 14–23, the next figures of the sequence provide meaningful information about the influence of another parameter, namely, the inclination of vibrations with respect to the y direction. While for Figs. 14–23, the angle formed by vibrations with the y direction was $\phi = 0$, in the remainder of this section the representative scenario where $\phi = 45°$ ($\pi/2$) is considered.

Along these lines, what stands immediately out from Fig. 24 for $l_s = 0.2$ is the observable change in the particle distribution, which may be considered somehow equivalent to that already reported by Lappa[28] in the case of uniformly heated walls; namely, the two otherwise parallel cylindrical structures with ellipsoidal cross section and axes parallel to the z direction are replaced by much more compact formation located in *opposite corners* of the cavity.

However, very interesting phenomena are produced for $l_s = 0.5$. In this specific case, the complexity of the pattern increases dramatically (see Fig. 25) and the hallmark of the emerging formation resides in its essentially cohesive (although extremely complex form a topological point of view) nature. In place of spatially segregated accumulations, a single entity is obtained, with a centrally symmetric morphology resembling that of a jellyfish. Indeed, the imaginative
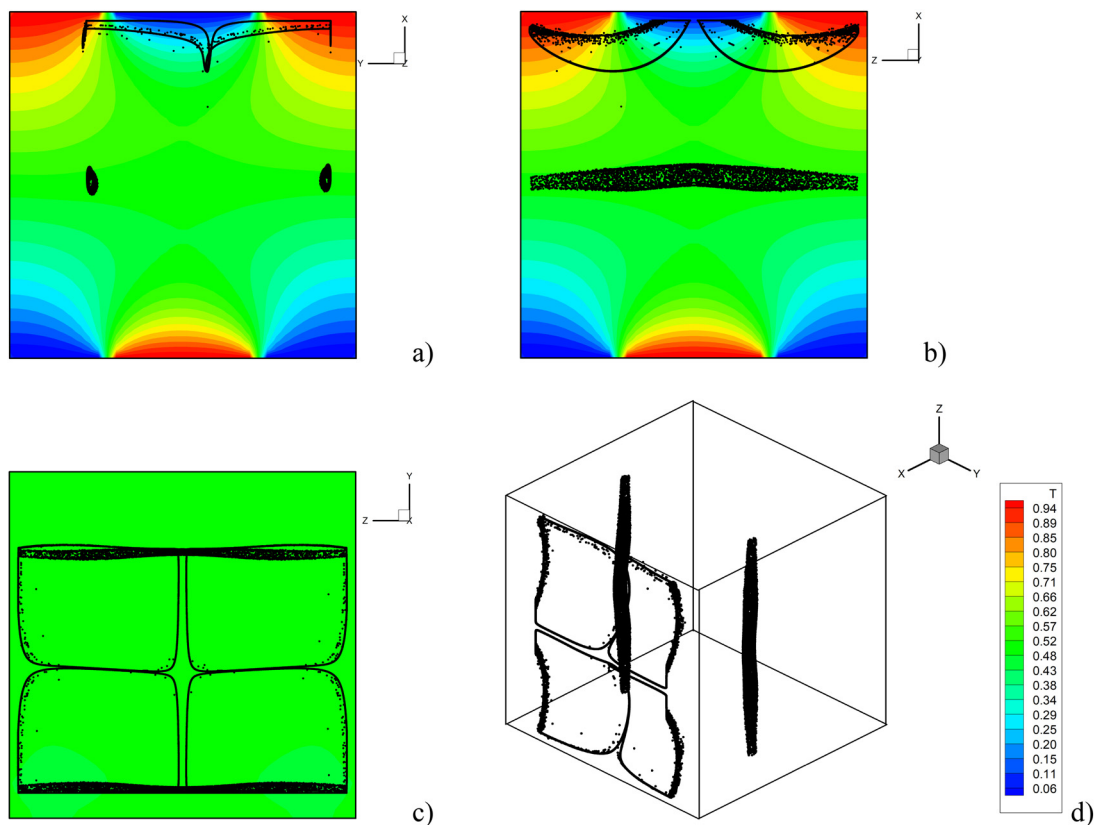

FIG. 26. Snapshot (3D views for $t \cong 8.96$) of particle structures and related temperature distribution for $\gamma = 1.5 \times 10^8$, $Ra_\omega = 10^4$, $\Omega = 10^3$, $St = 5 \times 10^{-6}$, $\xi = 2$, $\phi = 0°$, and $l_s = 0.4$: (a) perspective perpendicular to the xy mid-plane, (b) perspective perpendicular to the xz mid-plane, (c) perspective perpendicular to the yz plane, (d) isometric 3D view.

reader may distinguish a well-defined "cap" and distinct "tentacles" (Fig. 25). These, in turn, can be regarded as the natural evolution of the structures seen in Fig. 16 as the vibrations are rotated by 45° with respect to their original (y) direction.

5. Vibrational acceleration effects

In this subsection, following the same approach already implemented in Sec. IV A, the evolution in terms of patterning behavior is assessed with regard to another of the degrees of freedom of these systems, namely, their sensitivity to the magnitude of the vibrationally induced acceleration (body force). A first example of this assessment is shown in Fig. 26, where, in addition to a larger γ (1.5×10^8), a relatively high value of l_s is also considered ($l_s = 0.4$ and $\phi = 0$). Comparison with Fig. 15 immediately indicates that an increase in γ essentially produces a compaction of the particle accumulations (as expected their cross-sectional area becomes much smaller, i.e., the structures are thinner). Taken together, Figs. 15 and 26 also lead to the realization that for this value of γ, the quadrupolar pattern can be obtained for a value of l_s as small as 0.4 (not present for $l_s = 0.2$ and $\gamma = 1.5 \times 10^8$, not shown). However, unlike those seen in Fig. 16, in this case, no

breakage affects the two cylindrical central structures with axes parallel to the z direction, which reduces the multiplicity parameter to N = 6.

For a larger value of l_s (e.g., $l_s = 0.6$ in Fig. 27), interestingly, while the characteristic size (diameter) of the four formations pertaining to the aforementioned quadrupolar pattern is significantly lowered, the other two structures located in the bulk of the fluid display a different behavior; that is, they undergo a sort of compression or squeezing effect similar to that already reported for $\gamma = 10^8$, i.e., their extension along z is reduced, while their radial extension (as seen in the xy plane) grows. Although this has no impact on the multiplicity parameter (which is still N = 6), the quantitative changes affecting the pattern are remarkable. Opposite trends can indeed be noticed for the quadrupolar and central structures in terms of dependence of the related transverse size (internal diameter) on l_s. This is somehow reminiscent of the opposite tendencies already identified in the 2D case for the classical (boundary-dense) and the boundary-free accumulation regions. This observation reinforces our arguments that the underlying mechanisms are connected with the existence (during one cycle of modulation) of transitional convective stages of evolution (such as those shown in Fig. 10 for the 2D case and Fig. 19 for the 3D case), which do not exists when the cases with uniform heating are considered.
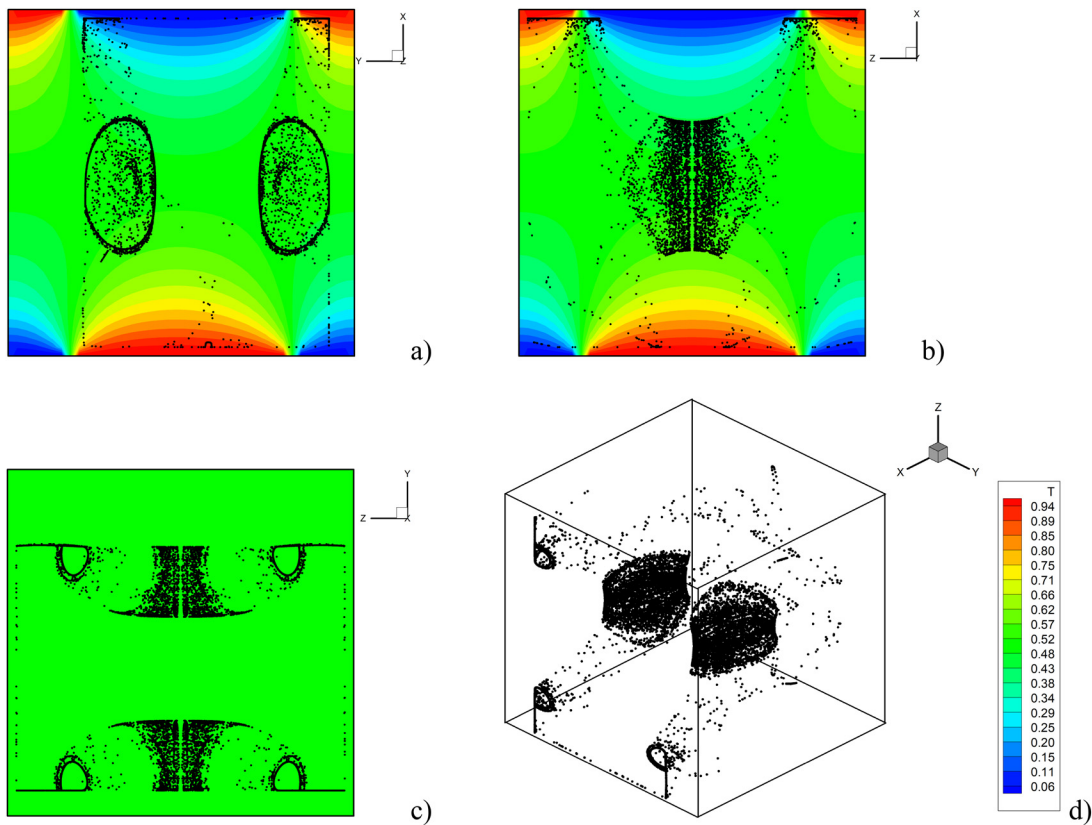

FIG. 27. Snapshot (3D views for $t \cong 8.96$) of particle structures and related temperature distribution for $\gamma = 1.5 \times 10^8$, $Ra_\omega = 10^4$, $\Omega = 10^3$, $St = 5 \times 10^{-6}$, $\xi = 2$, $\phi = 0°$, and $l_s = 0.6$: (a) perspective perpendicular to the xy mid-plane, (b) perspective perpendicular to the xz mid-plane, (c) perspective perpendicular to the yz plane, (d) isometric 3D view.

By analogy with what we have done in Sec. IV B 4, the next two figures of the sequence simply refer to the situation where the inclination of the vibrations is changed from $\phi = 0$ to $\phi = \pi/2$. In this regard, while Fig. 28 might be seen as the natural evolution of Fig. 26 as the parameter γ is increased, Fig. 29 provides some interesting insights *per se* (compare with Fig. 27). It indicates that, for $\phi = \pi/2$ (as opposed to $\phi = 0$ for Fig. 14), coalescence occurs between the four initially independent formations pertaining to the quadrupolar pattern and the "central" (standard) structures. Relatively, large conically shaped accumulations can be seen along a direction perpendicular to the yz plane, with two smaller cylindrical structures nested or embedded within each of them.

For the sake of completeness, the last figure deals with the corresponding changes that affect all these dynamics when γ is decreased (Fig. 30 is for $\gamma = 5 \times 10^7$, $\phi = 0$, and $l_s = 0.4$). Through comparison with the equivalent dynamics shown in Fig. 26 for $\gamma = 1.5 \times 10^8$, such a figure is instrumental in showing that, while, in general, an increase in γ results in compaction effects, vice versa, making it smaller can cause an expansion of the size of the structures with axes parallel to the z axis. Moreover, protuberances can originate from these structures, which extend *in a direction perpendicular to them* and ideally bridge their surface with the

aforementioned quadrupolar pattern [giving an external observer the illusion of a couple of hammer heads, Fig. 30(d)].

V. CONCLUSIONS

In order to upscale earlier findings related to relatively large particles and limited to a two-dimensional space, a new series of numerical simulations for relatively small (more realistic) values of the particle Stokes number have been conducted to explore the triadic relationship among the multiplicity and morphology of thermovibrationally driven particle attractors and the multi-directional nature of the imposed temperature gradient.

These computations have revealed new types of categories of particle accumulations differing with regard to the underlying mechanisms and the trends displayed in terms of size vs the different considered influential parameters.

Under the assumption of two-dimensional flow, a new class of formations shows up in certain ranges of the spot size relative dimension. These consist of solid mass-rich areas where particles are trapped as a consequence of the specific textural transitions undergone by the carrier thermovibrational flow during each cycle of vibrational modulation. The time during which particles are exposed to circulations of the type A (a single roll pervasive throughout the extension of the
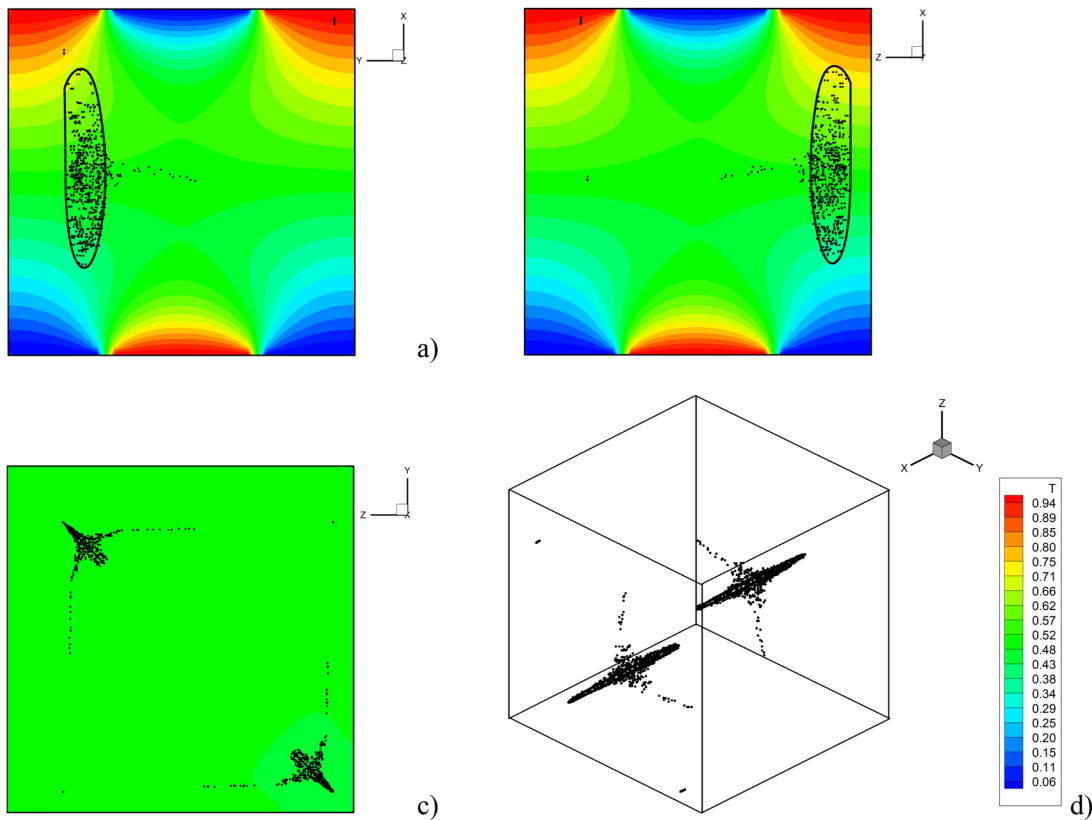

FIG. 28. Snapshot (3D views for $t \cong 8.96$) of particle structures and related temperature distribution for $\gamma = 1.5 \times 10^8$, $Ra_\omega = 10^4$, $\Omega = 10^3$, $St = 5 \times 10^{-6}$, $\xi = 2$, $\phi = 45°$, and $l_s = 0.4$: (a) perspective perpendicular to the xy mid-plane, (b) perspective perpendicular to the xz mid-plane, (c) perspective perpendicular to the yz plane, (d) isometric 3D view.
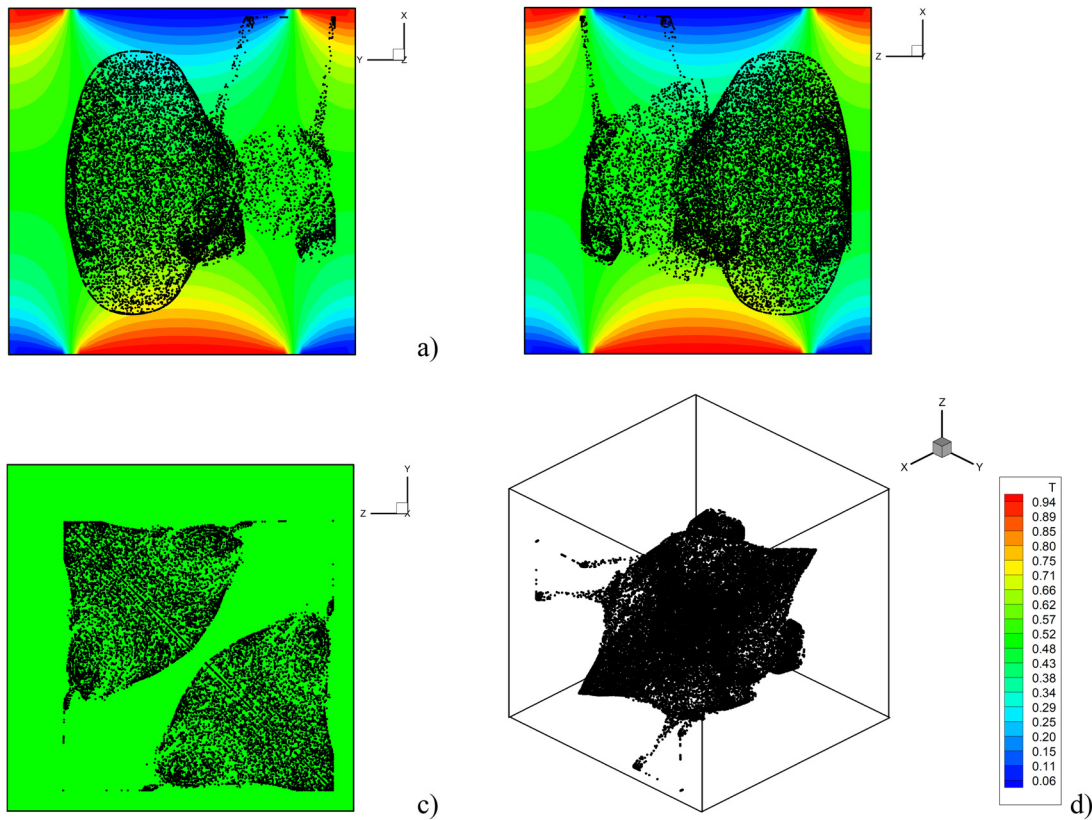
FIG. 29. Snapshot (3D views for $t \cong 8.96$) of particle structures for $\gamma = 1.5 \times 10^8$, $Ra_\omega = 10^4$, $\Omega = 10^3$, $St = 5 \times 10^{-6}$, $\xi = 2$, $\phi = 45°$, and $l_s = 0.6$: (a) perspective perpendicular to the xy mid-plane, (b) perspective perpendicular to the xz mid-plane, (c) perspective perpendicular to the yz plane, (d) isometric 3D view.

cavity) is not sufficient to allow drag-driven displacement of a certain portion of them to lateral regions where they can hit the sidewalls under the effect of the vibrationally induced body force acting on them. These particles are rather subjected to the action of alternate circulations and remain confined to a central region. Given their specific nature, the distinguishing mark of these accumulation regions is the lack of a well-defined particle-dense boundary separating them from the clear fluid outside.

If the constraint of two-dimensional flow is removed, other interesting phenomena become possible. In particular, for vibrations perpendicular to the sidewalls (case corresponding to a simple generalization of a 2D case to three dimensions), the increase in the multiplicity of the formations is essentially due to the manifestation of an additional set of apparently independent structures. These are still shaped in the form of cylindrical surfaces but display a relatively compact nature and axes parallel to the x direction (here simply referred to as "quadrupolar" pattern given the related intrinsic multiplicity). Accordingly, in some cases, the set of attractors can attain a degree of multiplicity as high as N = 8, corresponding in the physical space to four relatively extended cylindrical particle accumulation surfaces, each with a generatrix curve lying in the xy plane and other four relatively shallow formations with generatrix curves in the yz plane. As a common feature, and regardless of the degree of multiplicity N, the axes of all the emerging structures are always perpendicular to the

direction of the imposed vibrations (the y direction in the present case). Moreover, in analogy with the 2D circumstances, the additional formations contributing to increase the multiplicity parameter only exist in a given range of the parameter l_s (accounting for the relative extension of the temperature spot on the thermally controlled walls). These extra particle accumulations are essentially driven by the existence of a couple of counter-rotating vortices localized in proximity to the x = 1 plane.

Notably, a rotation by 45° in the shaking direction (vibrations contained in the xy plane) causes a compression of the structures and their *coalescence with the aforementioned quadrupolar sets*. This phenomenon can lead to a variety of fascinating and esthetically appealing compact realizations in terms of particle distribution inside the cavity, which further witness the possibility to use specific combinations of thermal boundary conditions and vibrational effects to force particles to form internal "frameworks" or "backbones" with desired shapes and degrees of topological complexity. Overall, this study should be seen as another step forward along the path heading to the acquisition of a "critical mass" of data for the development and training of an *algorithm of artificial intelligence*, that is, the ability (a kind of "reverse engineering") to determine for a desired (input) shape of the particle accumulation, the corresponding set of required (thermal) boundary conditions and mechanical stimuli.
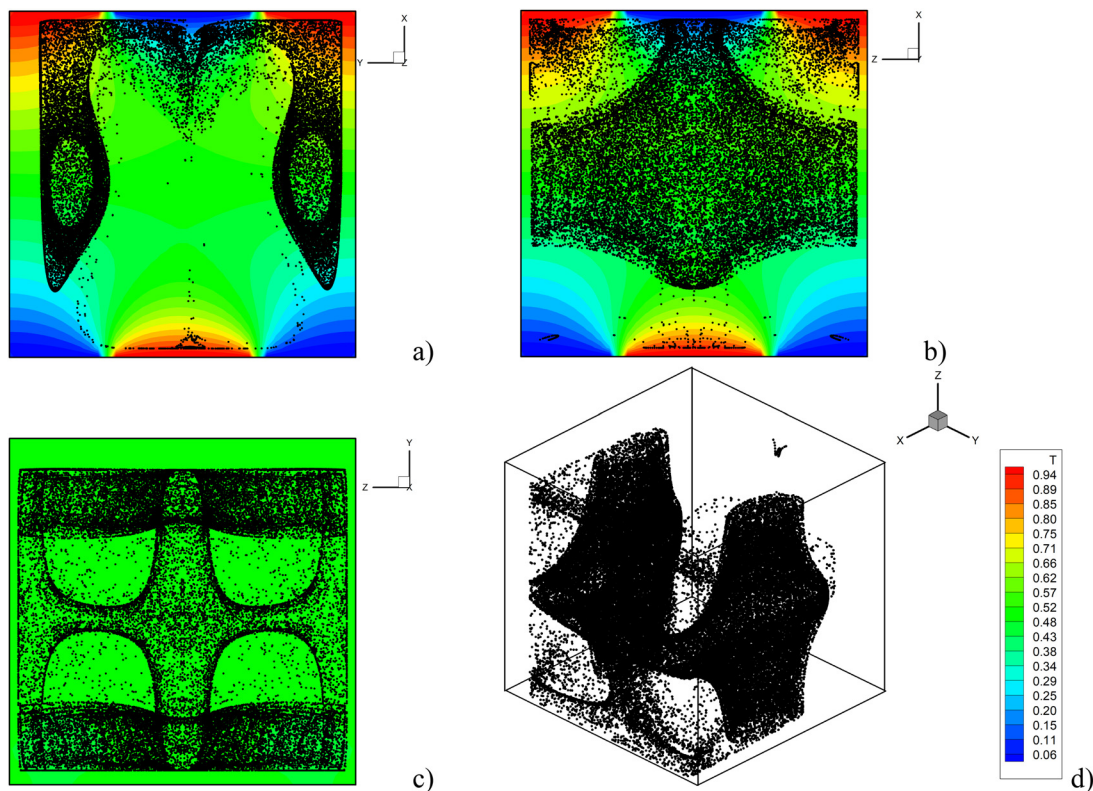
FIG. 30. Snapshot (3D views for $t \cong 8.96$) of particle structures and related temperature distribution for $\gamma = 5 \times 10^7$, $Ra_\omega = 10^4$, $\Omega = 10^3$, $St = 5 \times 10^{-6}$, $\xi = 2$, $\phi = 0°$, and $l_s = 0.4$: (a) perspective perpendicular to the xy mid-plane, (b) perspective perpendicular to the xz mid-plane, (c) perspective perpendicular to the yz plane, (d) isometric 3D view.

ACKNOWLEDGMENTS

AUTHOR DECLARATIONS
Conflict of Interest

The authors have no conflicts to disclose.

Author Contributions

Balagopal Manayil Santhosh: Data curation (lead); Investigation (equal); Resources (lead); Validation (lead); Visualization (lead); Writing – original draft (equal). **Marcello Lappa:** Conceptualization (lead); Formal analysis (lead); Funding acquisition (lead); Investigation (lead); Methodology (lead); Project administration (lead); Software (lead); Supervision (lead); Writing – original draft (equal).

DATA AVAILABILITY

The data that support the findings of this study are openly available in the Pure repository of the University of Strathclyde, at https://doi.org/10.15129/c12d9beb-8c56-4900-a74f-1395e5830ed4.

REFERENCES

[1]C. Wei, J. Wang, Y. He, J. Li, and E. Beaugnon, "Solidification of immiscible alloys under high magnetic field: A review," Metals **11**, 525 (2021).

[2]N. Gui, X. Li, and X. Tu, "Progress of particle flow, fluid/solid mechanics, and heat transfer in advanced gas/water nuclear reactors," Sci. Technol. Nucl. Installations **2016**, 512634.

[3]G. Li, J. Gao, P. Wen, Q. Zhao, J. Wang, J. Yan, and A. Yamaji, "A review on MPS method developments and applications in nuclear engineering," Comput. Methods Appl. Mech. Eng. **367**, 113166 (2020).

[4]J. Zong and J. Yue, "Continuous solid particle flow in microreactors for efficient chemical conversion," Ind. Eng. Chem. Res. **61**(19), 6269–6291 (2022).

[5]A. J. Rogers, A. Hashemi, and M. G. Ierapetritou, "Modeling of particulate processes for the continuous manufacture of solid-based pharmaceutical dosage forms," Processes **1**, 67–127 (2013).

[6]A. Rahmat, M. Barigou, and A. Alexiadis, "Numerical simulation of dissolution of solid particles in fluid flow using the SPH method," Int. J. Numer. Methods Heat Fluid Flow **30**(1), 290–307 (2019).

[7]D. V. Lyubimov, A. V. Straube, and T. P. Lyubimova, "Capture of particles of dust by convective flow," Phys. Fluids **17**, 063302 (2005).

[8]C. Sturtz, A. Limare, S. Tait, and É. Kaminski, "Birth and decline of magma oceans in planetesimals: 1. Experimental study of erosion and deposition of particles in an internally heated convecting fluid," JGR Planets **127**(12), e2021JE007000 (2022).

[9]D. V. Lyubimov, T. P. Lyubimova, and A. V. Straube, "Accumulation of solid particles in convective flows," Microgravity Sci. Technol. **16**, 210–214 (2005).

[10]D. Pushkin, D. Melnikov, and V. Shevtsova, "Ordering of small particles in one-dimensional coherent structures by time-periodic flows," Phys. Rev. Lett. **106**, 234501 (2011).

12 October 2023 08:29:15

[11]I. Ueno, "Experimental study on coherent structures by particles suspended in half-zone thermocapillary liquid bridges: Review," Fluids **6**(3), 105 (2021).

[12]M. Minale, R. Martone, and C. Carotenuto, "Microstructural changes of concentrated Newtonian suspensions in the first oscillation cycles probed with linear and non-linear rheology," Soft Matter **18**, 6051–6065 (2022).

[13]S. Terasaki, S. Sensui, and I. Ueno, "Thermocapillary-driven coherent structures by low-Stokes-number particles and their morphology in high-aspect-ratio liquid bridges," Int. J. Heat Mass Transfer **203**, 123772 (2023).

[14]T. P. Lyubimova, A. A. Fomicheva, and A. O. Ivantsov, "Dynamics of a bubble in oscillating viscous liquid," Philos. Trans. R. Soc. A: Math., Phys. Eng. Sci. **381**(2245), 20220085 (2023).

[15]M. Lappa, "On the nature of fluid-dynamics," in *Understanding the Nature of Science*, Science, Evolution and Creationism, editor by P. Lindholm (Nova Science Publishers Inc., 2019), Chap. 1, pp. 1–64.

[16]G. Haller and T. Sapsis, "Where do inertial particles go in fluid flows?," Phys. D **237**(5), 573–583 (2008).

[17]T. Sapsis and G. Haller, "Clustering criterion for inertial particles in two-dimensional time-periodic and three-dimensional steady flows," Chaos **20**, 017515 (2010).

[18]P. J. Ireland, A. D. Bragg, and L. R. Collins, "The effect of Reynolds number on inertial particle dynamics in isotropic turbulence. Part 2. simulations with gravitational effects," J. Fluid Mech. **796**, 617–658 (2016).

[19]K. Matsuda, K. Schneider, and K. Yoshimatsu, "Scale-dependent statistics of inertial particle distribution in high Reynolds number turbulence," Phys. Rev. Fluids **6**, 064304 (2021).

[20]D. Schwabe and A. I. Mizev, "Particles of different density in thermocapillary liquid bridges under the action of travelling and standing hydrothermal waves," Eur. Phys. J.: Spec. Top. **192**, 13–27 (2011).

[21]M. Lappa, "On the variety of particle accumulation structures under the effect of g-jitters," J. Fluid Mech. **726**, 160–195 (2013).

[22]M. Gotoda, D. E. Melnikov, I. Ueno, and V. Shevtsova, "Experimental study on dynamics of coherent structures formed by inertial solid, particles in three-dimensional periodic flows," Chaos **26**(7), 073106 (2016).

[23]D. E. Melnikov and V. Shevtsova, "Different types of Lagrangian coherent structures formed by solid particles in three-dimensional time-periodic flows," Eur. Phys. J.: Spec. Top. **226**(6), 1239–1251 (2017).

[24]P. Capobianchi and M. Lappa, "Particle accumulation structures in noncylindrical liquid bridges under microgravity conditions," Phys. Rev. Fluids **5**(8), 084304–084330 (2020).

[25]P. Capobianchi and M. Lappa, "On the influence of gravity on particle accumulation structures in high aspect-ratio liquid bridges," J. Fluid Mech. **908**, A29 (2021).

[26]R. Parker, P. Capobianchi, and M. Lappa, "Competing particle attractee in liquid bridges," Philos. Trans. A **381**(2244), 20220302 (2023).

[27]M. Lappa, "The patterning behavior and accumulation of spherical particles in a vibrated non-isothermal liquid," Phys. Fluids **26**(9), 093301 (2014).

[28]M. Lappa, "On the multiplicity and symmetry of particle attractors in confined non-isothermal fluids subjected to inclined vibrations," Int. J. Multiphase Flow **93**, 71–83 (2017).

[29]M. Lappa, "On the formation and morphology of coherent particulate structures in non-isothermal enclosures subjected to rotating g-jitters," Phys. Fluids **31**(7), 073303 (2019).

[30]M. Lappa and T. Burel, "Symmetry breaking phenomena in thermovibrationally driven particle accumulation structures," Phys. Fluids **32**(5), 053314 (2020).

[31]M. Lappa, T. Burel, M. Kerr, G. Crewdson, A. Boaro, P. Capobianchi, S. V. Bonnieu, L. Murphy, P. Randall, and S. Hens, "Particle vibration, an instrument to study particle accumulation structures on board the International Space Station," Microgravity Sci. Technol. **34**(3), 33 (2022).

[32]G. Crewdson, M. Evans, and M. Lappa, "Two-dimensional vibrationally-driven solid particle structures in non-uniformly heated fluid containers," Chaos **32**(10), 103119 (2022).

[33]L. Ratke, G. Korekt, and S. Drees, "Phase separation and solidification of immiscible metallic alloys under low gravity," Adv. Space Res. **22**(8), 1227–1236 (1998).

[34]M. Lappa, "Assessment of VOF strategies for the analysis of Marangoni migration, collisional coagulation of droplets and thermal wake effects in metal alloys under microgravity conditions," Comput., Mater. Continua **2**(1), 51–64 (2005).

[35]M. Lappa, C. Piccolo, and L. Carotenuto, "Numerical and experimental analysis of periodic patterns and sedimentation of lysozyme," J. Cryst. Growth **254**(3–4), 469–486 (2003).

[36]M. Lappa and D. Castagnolo, "Complex dynamics of rhythmic patterns and sedimentation of organic crystals: A new numerical approach," Num. Heat Transfer Part B **43**(4), 373–401 (2003).

[37]G. Crewdson and M. Lappa, "An investigation into the behavior of non-isodense particles in chaotic thermovibrational flow," Fluid Dyn. Mater. Process **18**(3), 497–510 (2022).

[38]V. Shevtsova, T. Lyubimova, Z. Saghir *et al.*, "IVIDIL: On-board g-jitters and diffusion controlled phenomena," J. Phys. Conf. Ser. **327**(1), 012031 (2011).

[39]M. Lappa, "Characterization of two-way coupled thermovibrationally driven particle attractee," Phys. Fluids **34**(5), 053109–053127 (2022).

[40]R. Clift, J. R. Grace, and M. E. Weber, *Bubbles, Drops, and Particles* (Courier Corporation, 2005).

[41]P. M. Gresho, "Incompressible fluid dynamics: Some fundamental formulation issues," Ann. Rev. Fluid Mech. **23**, 413–453 (1991).

[42]O. A. Ladyzhenskaya, *The Mathematical Theory of Viscous Incompressible Flow*, 2nd ed. (Gordon and Breach, New York, London, 1969).

[43]M. Lappa, "Numerical study into the morphology and formation mechanisms of three dimensional particle structures in vibrated cylindrical cavities with various heating conditions," Phys. Rev. Fluids **1**(6), 064203 (2016).

[44]G. Crewdson and M. Lappa, "Three-dimensional solid particle self-assembly in thermovibrational flow: The case with unidirectional temperature gradient and concurrent vibrations," Phys. Fluids **35**(2), 023323 (2023).